Author Manuscript

Author Manuscript

Author Manuscript

Author Manuscript

HHS Public Access

Author manuscript

Mol Cell. Author manuscript; available in PMC 2021 October 01.

Published in final edited form as:

Mol Cell. 2020 October 01; 80(1): 140–155.e6. doi:10.1016/j.molcel.2020.09.007.

Overlapping activities of ELAV/Hu family RNA binding proteins specify the extended neuronal 3' UTR landscape in *Drosophila*

Lu Wei[1,5], **Seungjae Lee**[1,5], **Sonali Majumdar**[1], **Binglong Zhang**[1], **Piero Sanfilippo**[1,2], **Brian Joseph**[1,2], **Pedro Miura**[1,3], **Matthias Soller**[4], **Eric C. Lai**[1,6]

[1]Department of Developmental Biology, Sloan-Kettering Institute, New York, NY 10065 USA

[2]Louis V. Gerstner, Jr. Graduate School of Biomedical Sciences, Memorial Sloan Kettering Cancer Center, New York, NY 10065 USA

[3]Department of Biology, University of Nevada, Reno, Reno, NV, 89557 USA

[4]School of Biosciences, College of Life and Environmental Sciences, University of Birmingham, Edgbaston, Birmingham, United Kingdom

[5]These authors contributed equally

[6]Lead Contact

Summary

The tissue-specific deployment of highly extended neural 3' UTR isoforms, generated by alternative polyadenylation (APA), is a broad and conserved feature of metazoan genomes. However, the factors and mechanisms that control neural APA isoforms are not well-understood. Here, we show that three ELAV/Hu RNA binding proteins (Elav, Rbp9 and Fne) have similar capacities to induce a lengthened 3' UTR landscape in an ectopic setting. These factors promote accumulation of chromatin-associated, 3' UTR-extended, nascent transcripts, through inhibition of proximal polyadenylation site (PAS) usage. Notably, Elav represses an unannotated splice isoform of *fne*, switching the normally cytoplasmic Fne towards the nucleus in *elav* mutants. We use genomic profiling to reveal strong and broad loss of neural APA in *elav/fne* double mutant CNS, the first genetic background to largely abrogate this distinct APA signature. Overall, we demonstrate how regulatory interplay and functionally overlapping activities of neural ELAV/Hu RBPs drives the neural APA landscape.

Graphical Abstract

ph: 212-639-5578, laie@mskcc.org.

Author Contributions

Conceptualization: LW, SL, SM, PS and ECL. Experimental analysis (LW: cell and molecular assays, CNS libraries; SM: initial studies and S2 libraries; BZ: CNS dissection and immunostaining). Computational analysis: SL. Methodology: PS, BJ and PM. Resources: MS. Writing - Original Draft: ECL. Writing - Review and Editing: All authors. Supervision, Project Administration, Funding Acquisition: ECL.

Publisher's Disclaimer: This is a PDF file of an unedited manuscript that has been accepted for publication. As a service to our customers we are providing this early version of the manuscript. The manuscript will undergo copyediting, typesetting, and review of the resulting proof before it is published in its final form. Please note that during the production process errors may be discovered which could affect the content, and all legal disclaimers that apply to the journal pertain.

Declaration of Interests

The authors declare no competing interests.

Author Manuscript Author Manuscript Author Manuscript Author Manuscript

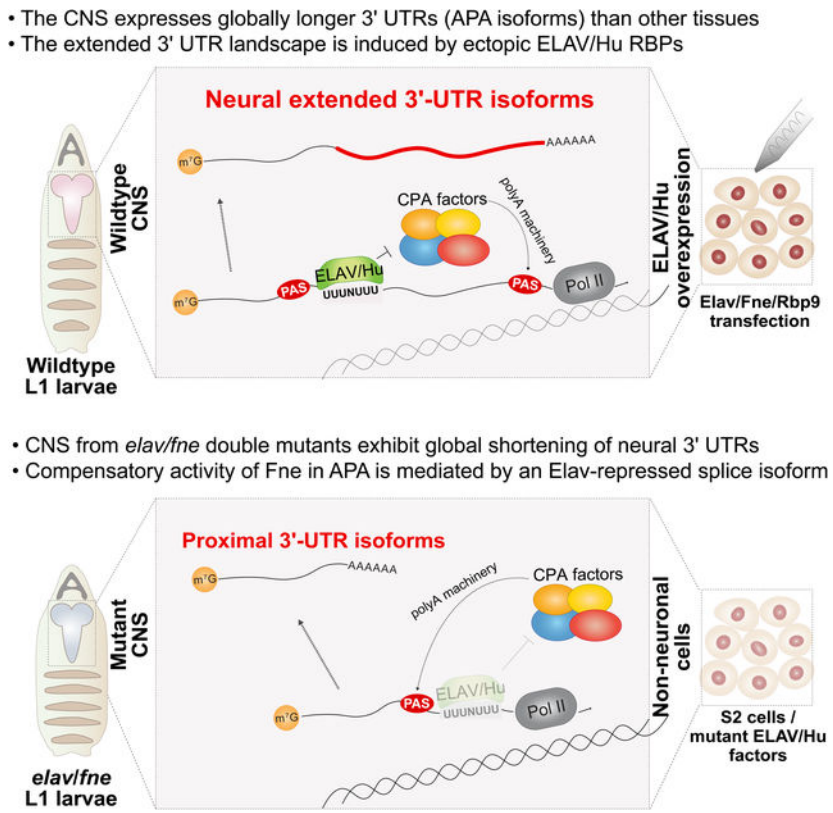

eTOC blurb:

Neurons express much longer 3’ UTRs than other celltypes. Here, Wei and Lee et al. determine that roles of *Drosophila* ELAV/Hu RNA binding proteins are necessary and sufficient to determine the extended 3’ UTR landscape. Moreover, their compensatory functions involve splicing and subcellular regulation between ELAV/Hu members.

Introduction

The 3’ untranslated region (UTR) is the major hub for post-transcriptional control, and harbors elements that direct regulation by RNA binding proteins (RBPs), miRNAs, and RNA modifications. Such regulatory elements can be rendered conditional by alternative polyadenylation (APA), which yields 3’ UTR diversity from an individual locus (Tian and Manley, 2017). Most eukaryotic genes accumulate distinct 3’ UTR isoforms, and this can be influenced by differentiation status, tissue identity, environmental and metabolic conditions (Gruber and Zavolan, 2019). Moreover, APA is broadly disregulated in disease and cancer, and may help to drive aberrant gene expression states (Masamha and Wagner, 2018).

Many tissues generate characteristic APA landscapes, implying that developmental factors regulate 3’ UTR programs. A striking example involves the nervous system, where many hundreds of genes express substantially longer 3’ UTRs compared to other tissues (Lianoglou et al., 2013; Miura et al., 2013; Smibert et al., 2012; Tian et al., 2005; Zhang et al., 2005). Many of these neural 3’ UTR extensions are extremely lengthy, and we validated

Author Manuscript Author Manuscript Author Manuscript Author Manuscript

stable isoforms bearing ~20 kb 3’ UTRs in flies (Smibert et al., 2012) and mice (Miura et al., 2013) by Northern blot. Despite the breadth and conservation of this phenomenon, and functional studies that link neural-specific 3’ UTRs to splicing choice, transcript localization, local translation, and miRNA regulation (An et al., 2008; Blair et al., 2017; Garaulet et al., 2020a; Kuklin et al., 2017; Yudin et al., 2008; Zhang et al., 2019), relatively little is known of mechanisms that determine neural-extended 3’ UTR isoforms.

Several identified APA mechanisms modulate the levels or activities of cleavage and polyadenylation factors (Lackford et al., 2014; Takagaki et al., 1996; Yang et al., 2020; Zhu et al., 2018). For example, interaction of U1 snRNP with polyA factors plays a major role in inhibiting premature 3’-end processing (Berg et al., 2012; Gunderson et al., 1998). Other mechanisms that impact polyA site choice include recruitment of polyA factors at promoters (Calvo and Manley, 2001; Dantonel et al., 1997; Ji et al., 2011) and RNA Pol II speed (Pinto et al., 2011). However, there is growing appreciation that local recruitment of RBPs can affect polyA site recognition or regulate later steps to inhibit cleavage and polyadenylation (Batra et al., 2014; Chatrikhi et al., 2019; Gruber et al., 2016; Jenal et al., 2012).

Amongst RBPs with roles in APA are certain members of the ELAV/Hu family, of which there are four in human (HuR and HuB-D) and three in *Drosophila* (Elav, Fne and Rbp9). All are expressed in neurons, but HuB and RBP9 are also expressed in gonads and HuR is ubiquitous (Soller and White, 2004). *Drosophila* Elav was shown to regulate APA at *erect wing* (*ewg*), where it binds U-rich motifs distal of the cleavage site and inhibits 3’-end processing (Soller and White, 2003, 2005). Likewise, all four mammalian Hu proteins suppress an intronic polyA site in *calcitonin/CGRP*, and *HuR* autoregulates by APA (Dai et al., 2012; Mansfield and Keene, 2012; Zhu et al., 2007). In addition, HuR regulates 3’-end processing of several membrane proteins (Berkovits and Mayr, 2015). Given the predominant neuronal expression of many ELAV/Hu members, these proteins are candidate regulators of CNS-specific 3’ UTR extensions. Elav mediates neural 3’ UTR extensions of certain genes (Hilgers et al., 2012), but the breadth of Elav involvement in the neuronal APA landscape has not been investigated.

To gain a comprehensive understanding of ELAV/Hu RBPs in 3’ UTR isoform regulation, we applied genomic approaches using gain- and loss-of-function genetics. Surprisingly, we find that *elav* knockouts are not strictly embryonic lethal, as long believed, nor is Elav essential for most neural 3’ UTR extensions to accumulate. Using a heterologous system we find all three *Drosophila* ELAV/Hu RBPs (Elav, Fne and Rbp9) have similar capacities to broadly induce a neural 3’ UTR extension landscape. They do so by promoting bypass of proximal polyadenylation signals (PAS) in nascent transcripts. Although Elav is normally the predominant nuclear Hu factor in *Drosophila*, we find that in *elav* null CNS, the normally cytoplasmic Fne protein becomes substantially nuclear, owing to induction of a previously unrecognized splice isoform. Accordingly, genomic analyses of *elav/fne* double mutant CNS reveal strong loss of neural 3’ UTR extensions. Overall, we demonstrate critical overlapping roles for ELAV/Hu RBPs to generate the neural-extended 3’ UTR landscape.

Author Manuscript Author Manuscript Author Manuscript Author Manuscript

RESULTS

Elav is not essential for the accumulation of neural 3' UTR extensions

Elav is an acronym for "embryonic lethal, abnormal vision", and it is the ony *Drosophila* Hu family member required for viability (Campos et al., 1985). Consequently, prior molecular analyses of 3' UTR isoforms in *elav* mutants utilized embryos (Hilgers et al., 2012; Oktaba et al., 2015). Unexpectedly, we discovered that *elav[5]* null mutants are not embryonic lethal *per se*. Upon liberating them from the eggshell, we obtained viable, although highly locomotor-defective, 1st instar (L1) mutant larvae (Figure 1A). Notably, qPCR analysis of 3' UTR extensions described as fully Elav-dependent (Hilgers et al., 2012; Oktaba et al., 2015) revealed highly selective effects at L1. Of these, *pum* exhibited loss of a distal 3' UTR extension in *elav* null mutants while *imp* showed a partial reduction; *brat*, *nej*, *mei-P26* and *ago1* expressed 3' UTR extensions in *elav[5]* larvae (Figure 1B).

To gain increased specificity, higher resolution and broader perspectives, we generated RNA-seq data from control and *elav[5]* dissected larval CNS (Table S1). While CNS contains non-neural cells, we showed that bulk head RNA exhibits strong switches to neural-extended isoforms (Sanfilippo et al., 2017b; Smibert et al., 2012); thus, neural isoforms make substantial contributions to total transcripts in *Drosophila* CNS. This is relevant, as qPCR of proximal 3' UTR amplicons reflects expression of both universal and extended isoforms, which are expected to be dominated by contributions from non-neural tissues when assaying embryos (Hilgers et al., 2012; Oktaba et al., 2015) or whole larvae (Figure 1B). Purity of our mutant CNS dissections was evident by inspecting the *elav* locus (Figure 1C). Consistent with *elav[5]* being a deletion allele (Robinow and White, 1991), mutant embryos lack transcripts from the coding and bulk UTR regions, although we observed a low level of a very distal *elav* 3' UTR segment (Figure 1C). Nevertheless, even when analyzing CNS-specific RNA, the previously assayed Elav-dependent 3' UTR extensions (Hilgers et al., 2012; Oktaba et al., 2015) were only partially or not affected in *elav[5]* null mutants (Figure 1D and Figure S1). Thus, although Elav was reported as a master regulator of neural 3' UTR extensions, it is not essential for many neural 3' UTRs to accumulate *in vivo*.

Ectopic Elav is sufficient to induce accumulation of extended 3' UTR isoforms

Misexpression of Elav in embryos can induce ectopic neural 3' UTR extensions of *brat* (Hilgers et al., 2012) and *elav* itself (Oktaba et al., 2015). To test this concept more broadly, we used a cell-based system to investigate ELAV/Hu family activities. While Elav is known as a canonical marker of post-mitotic neurons, it is detectably transcribed and translated ubiquitously (Sanfilippo et al., 2016). However, this low level of non-neural *elav* is suppressed by miRNAs. Thus, despite modest levels of Elav protein in hemocyte-like S2R+ cells (Sanfilippo et al., 2016), it is straightforward to elevate Elav in these cells. Accordingly, we found that ectopic Elav lengthens the *Dscam1* 3' UTR in S2 cells (Zhang et al., 2019).

For further tests, we introduced point substitutions in all 3 RNA recognition motifs (RRMs) of Elav, using mutations known to impair its RNA-binding activity (Lisbin et al., 2001). We transfected *actin* promoter-driven Flag-HA tagged constructs for Elav-WT or 3X-RRM

Author Manuscript Author Manuscript Author Manuscript Author Manuscript

mutant (Elav-MT) into S2R+ cells, yielding similar accumulation of ~55 kDa Elav proteins (Figure 2B). We assayed effects on endogenous transcripts using Northern blotting, which resolves multiple stable isoforms. Elav-WT, but not 3x-RRM, induced the accumulation of neural-like 3' UTR extension isoforms for *Goα−47A* and *AcCoAs* (Figure 2C). Thus, Elav is sufficient to induce extended 3' UTRs.

Elav paralogs Fne and Rbp9 also induce specific accumulation of extended 3' UTRs

To address why Elav is sufficient, but seemingly not essential, for neural APA, we considered its paralogs, Found in neurons (Fne) and RNA binding protein 9 (Rbp9). These factors received comparably little attention since their mutants are viable and appear largely normal, although *fne* mutants exhibit specific adult behavioral defects (Zaharieva et al., 2015; Zanini et al., 2012) and *rbp9* mutants have oogenesis defects (Kim-Ha et al., 1999). While Fne and Rbp9 may simply have different biochemical functions than Elav, it cannot be overlooked that all three Hu members are substantially restricted to neurons (Kim and Baker, 1993; Samson and Chalvet, 2003).

We conducted sufficiency tests of wildtype and 3X-RRM mutant versions of Fne and Rbp9 in S2R+ cells. The wildtype and mutant versions of either Hu factor accumulated similarly by Western blot (Figure 2B). Notably, Fne and Rbp9 both induced the same 3' UTR isoform extensions as did Elav, while their mutant counterparts were inert (Figure 2C).

The fact that Elav, Rbp9, and Fne can all bind similar U-rich sequences *in vitro* (Zaharieva et al., 2015) provides a rationale for why they may have similar biochemical activity, especially in ectopic settings. However, this also raised a question of specificity. In particular, can any U-rich RNA binding protein induce 3' UTR lengthening? This was germane, since the closest relative of ELAV/Hu factors, Sxl, also binds U-rich sequences and can influence splicing of Elav targets when ectopically expressed (Zaharieva et al., 2015). To address this, we analyzed U-rich RBPs Sxl, its paralog Ssx, and hnRNP-C. However, even though hnRNP-C (Fischl et al., 2019; Gruber et al., 2016) and Sxl (Gawande et al., 2006) are APA factors, none of these induced long 3' UTR isoforms (Figure 2B–C). We extended these tests by assaying universal and extended 3' UTRs amplicons for 9 additional loci. Only wild type ELAV/Hu factors induced 3' UTR extensions, while neither their mutant counterparts, nor hnRNP-C, Sxl or Ssx, had such capacity (Figure 2D and Figure S2). Altogether, we conclude that multiple ELAV/Hu family members share specific activities to remodel overlapping sets of endogenous transcripts towards the neural landscape.

Global extension of the 3' UTR landscape by three *Drosophila* ELAV/Hu family RBPs

To extend these observations genome-wide, we generated 3'-seq and RNA-seq from naive S2R+ cells expressing wildtype Elav/Fne/Rbp9 or their respective 3xRRM-mut variants (Table S1). PCA analysis showed that mutant ELAV/Hu RBPs only mildly shifted their profile from S2R+ cells, while all wildtype ELAV/Hu RBPs induced dramatic and overlapping alterations (Figure 3A). Inspection of genome browser tracks showed that this was due to broad and common induction of 3' UTR extended isoforms by wildtype ELAV/Hu RBPs, whereas their mutant counterparts resembled control cells (Figure 3B and Figure S3). To determine if Hu RBPs induced global directional changes in length isoforms,

Author Manuscript Author Manuscript Author Manuscript Author Manuscript

we performed two analyses. First, we calculated the expression of distal 3' UTR regions across replicates and compared these values between conditions (Table S2). This revealed highly directional shifts in that each wildtype ELAV/Hu RBP preferentially induced lengthened 3' UTR isoforms across hundreds of loci (Figure 3C–E).

Another way to view APA shifts is to calculate 3' UTR weighted lengths (Sanfilippo et al., 2016), which provides an average 3' UTR length for each gene calculated in proportion to 3'-seq depths for each APA isoform. This metric has the disadvantage of underestimating aspects of APA changes. For example, if the distal extension is a minor isoform, it may not substantially alter the weighted 3' UTR length, even though it may go from being completely absent to present between conditions. On the other hand, this metric is useful to isolate loci that undergo largescale shifts in 3' UTR real estate, characteristic of neural APA. Notably, if the alternate 3' ends are not very far apart, even complete switching of 3' UTR isoforms between samples will not generate a large difference in weighted 3' UTR lengths.

Analyzing weighted 3' UTR lengths (Table S3), we clearly observe that all three wildtype Hu RBPs reproducibly induced strongly directional shifts toward longer 3' UTRs, with relatively few loci exhibiting shortening (Figure 3F–H). By contrast, Elav/RBP/Fne-3xRRM mutants exhibited global 3' UTR profiles that were not substantially different from S2R+ cells, by either distal 3' UTR usage or weighted 3' UTR length metrics (Figure 3I–K).

Consistent with Northern and qPCR analyses (Figure 2), the behavior of individual loci was largely overlapping amongst Elav/Rbp9/Fne. Moreover, the new distal ends promoted by ectopic ELAV/Hu factors were not just any termini, but a majority corresponded to distal ends utilized in neural tissues (Figure 3B and Figure S3). Altogether, ectopic Elav/Rbp9/Fne have similar capacities to broadly transform the 3' UTR landscape of a non-neural cell type towards the neural state.

Hu family RBPs increase distal 3' UTR isoforms at the nascent transcript level

Elav suppresses 3'-end cleavage at proximal alternative last exon splicing isoforms of *ewg* and *nrg* (Lisbin et al., 2001; Soller and White, 2003), and at selected tandem 3' UTR events (Hilgers et al., 2012). However, given that Hu-type U-rich binding sites are frequent in *Drosophila* 3' UTRs (Sanfilippo et al., 2017b), and mammalian Hu proteins are known to confer target stability (Mirisis and Carew, 2019), an alternative model is that Hu proteins might induce 3' UTR extension isoforms by promoting their stability. We used S2R+ cells to test how *Drosophila* ELAV/Hu RBPs remodel 3' UTR isoforms (Figure 4A).

We first assessed effects on gene expression. If *Drosophila* ELAV/Hu RBPs globally induce extension isoforms by affecting their stability, we might expect a correlation between effects on APA and gene expression. We used 3'-seq data to quantify gene expression differences in replicates of Elav, Rbp9 and Fne misexpression. Each of these induced a biased profile with more upregulated than downregulated genes. However, in all cases, these gene expression changes were largely not correlated with induction of 3' UTR extension isoforms, which were largely unchanged and were not biased with respect to their direction of expression change (e.g. Figure 4B).

Author Manuscript Author Manuscript Author Manuscript Author Manuscript

We next tested effects on subcellularly localized transcripts. If ELAV/Hu RBPs largely mediate stability effects, we might expect to see specific effects on cytoplasmic transcripts. However, if their primary roles are to regulate 3' end processing, then we may also see companion effects in nuclear and/or chromatin fractions. We isolated these fractions from cells overexpressing *Drosophila* ELAV/Hu RBPs. Although Elav is predominantly nuclear and Fne/Rbp9 mostly cytoplasmic, we could detected transfected proteins in both compartments. This was consistent with their known shuttling behavior (Zaharieva et al., 2015), but the relevant issue of endogenous Hu RBP localization is addressed later.

Using these preparations, we conducted qPCR assays of universal and extension amplicons. Elav/Rbp9/Fne specifically induced 3' UTR extension isoforms for *AcCoAs*, *Goα−47A* and *put* in both cytoplasmic and nuclear fractions, while U-rich binding protein Sxl did not (Figure S4). As these data were consistent with a general effect on nuclear processing, we analyzed the chromatin fraction further. To validate the fractionations, we assayed protein-coding *gapdh1* and *rp49* transcripts, which were enriched in cytoplasmic RNA as expected. In contrast, the nuclear RNAs *roX1* and *roX2*, which coat the male X chromosome during dosage compensation (Franke and Baker, 1999; Kelley et al., 1999) were enriched in both nuclear and chromatin fractions from (male) S2R+ cells (Figure 4C). Using these materials, we observed that ectopic Elav/Rbp9/Fne all increased the levels of 3' UTR extension isoforms of eight genes in chromatin-associated RNAs, as normalized to *roX2* (Figures 4D and S5). Finally, we assessed nascent transcripts isolated from 4sU-labeling. In all four cases tested, we observed that only wild-type Elav/Rbp9/Fne, and not their RRM-mutant versions, had common abilities to increase the levels of newly-transcribed 3' UTR extension isoforms (Figure 4E).

Altogether, these tests indicate that ELAV/Hu RBPs generally re-wire the APA isoform landscape by driving the production of 3' UTR extension isoforms in the nascent and chromatin-associated transcript pools, consistent with impacts on suppressing cleavage of proximal 3' UTR isoforms.

ELAV/Hu family RBPs directly mediate bypass of polyA sites with distinct features

We investigated the features of 3' termini in genes subject to ELAV/Hu RBP-mediated 3' UTR lengthening. Genes that maintain only a single end, even in the presence of ectopic ELAV/Hu RBPs, comprise one class of robust termini. As most genes exhibit multiple 3'-ends, especially following ELAV/Hu RBP gain-of-function, we categorized 3'-ends according to their relative positions. We assigned "dominant universal ends" as those termini with highest expression level in control S2R+ cells. Ends detected upstream of the universal ends were termed "proximal" ends. Those downstream were termed "extension-terminal" if they were the final or only distal end, with the remainder grouped as "extension-internal" ends (Figure 5A). Note that the proximal and extension-internal categories are expected to include termini of heterogenous usage (e.g., including biochemically valid, but perhaps fortuitous ends), whereas the universal and extension-terminal categories comprise clearly well-utilized and/or final sites for most genes.

We first assessed the quality of core polyadenylation signal (PAS) motifs at these different categories of sites. The single-end termini set a baseline for this analysis (Figure 5B), with

Author Manuscript Author Manuscript Author Manuscript Author Manuscript

~83% of ends utilizing high-quality PAS (mostly canonical AAUAAA, less frequently AUUAAA or AAUAUA). When analyzing multi-end genes whose 3' distribution was not altered by ectopic Elav, we observed that universal ends exhibited high PAS quality similar to termini at single-end genes, while the extension-terminal sites of these loci were of noticeably lower overall quality (Figure 5C). The other categories of 3' ends exhibited even lower PAS quality. By contrast, the PAS sites in genes subject to 3' UTR extension exhibited reversed features in their universal vs. extension-terminal sites, with the latter exhibiting markedly higher quality (Figure 5C). We observed similar patterns when analyzing the Fne-extended and Rbp9-extended loci (Figure 5D–E). These data are consistent with the notion that cleavage sites bypassed by Elav/Fne/Rbp9 are moderately weak 3' termini. However, these differences were not sufficient to explain the specificity of ELAV/Hu factor actions.

We assessed other *cis*-motifs associated with PAS that were bypassed by ectopic Hu proteins. When we performed de novo motif searches of the regions downstream of single-end genes, we recovered a U/GU-rich motif (Figure 5F). This was reminiscent of the presence of the downstream U-rich element (DUE) in different metazoans (Gruber and Zavolan, 2019; Tian and Manley, 2017), which coincides with the U/GU-rich CstF64/CstF64τ binding site (Yao et al., 2012). However, we obtained a distinct U-rich motif downstream of proximal PAS that were bypassed in the presence of Elav/Fne/Rbp9 (Figure 5F). Besides A-rich sequences, these U-rich motifs were the top-enriched motifs in 50-nt windows downstream of bypassed PAS. Notably, these closely matched the sites for Elav, Fne and Rbp9 identified using *in vitro* selection (Ray et al., 2013) (Figure 5F).

We used position weight matrices (PWMs) for Elav/Fne/Rbp9 (Ray et al., 2013) and plotted their locations with respect to cleavage sites. To correlate this with the inferred effect on Elav/Fne/Rbp9 on inducing bypass at any particular cleavage site, we calculated the bypass ratio (Figure 5A). In brief, we determined a bypass score for each cleavage site, which corresponds to the percentage of 3'-seq reads downstream of a given 3' end, out of total 3'-seq reads for that transcript. To compare the behavior of a 3' end between samples (e.g., between wt and RRM-mutant versions of a given Hu paralog), we calculated the ratio of bypass scores at that site (Figure 5A). This does not reflect cleavage strength perfectly, because these scores might be affected by differential gene expression between samples. However, as levels of ELAV/Hu-responsive APA transcripts are not strongly or directionally affected (Figure 4A), it is a reasonable inference. These analyses showed that cleavage sites that were most bypassed by ectopic Elav/Fne/Rbp9 all showed enrichment for their cognate binding sites just downstream (Figure 5G–I).

These data indicate that Elav/Fne/Rbp9 have general and direct impacts to promote 3' end bypass, by preferentially associating downstream of genes with weaker core PAS.

Nuclear relocalization of Fne protein in *elav* mutant larval CNS

Multiple Hu family proteins have similar capacities to induce the neural APA landscape in an ectopic setting. Do these data help address our original conundrum that *elav* knockout CNS exhibits only mild trends for decreased levels of neural 3' UTR extensions (Figure 1)?

Author Manuscript Author Manuscript Author Manuscript Author Manuscript

We considered the temporal deployment of these factors using public data (Brown et al., 2014). As noted (Sanfilippo et al., 2016; Zaharieva et al., 2015), *elav* is detected throughout embryogenesis and early larval stages, but peaks during mid-embryo stages when the nervous system is specified (Figure S6). By comparison, the proiles *fne* and *rbp9* are temporally delayed, but by late embryogenesis and L1, the transcript levels of all three ELAV/Hu factors are comparable. However, as we found that *elav* is subject to substantial post-transcriptional repression (Sanfilippo et al., 2016), their relative protein levels are more relevant.

Inspection of developmental proteome data (Casas-Vila et al., 2017) revealed more exaggerated differences than was apparent from RNA-seq. Elav was highly abundant across the latter half of embryogenesis, consistent with the long history of Elav antibodies as a pan-neuronal marker (Robinow and White, 1991). By contrast, Fne was only detected by the end of embryogenesis, while Rbp9 was not detected above background in embryos. In whole L1 larvae, Elav protein remained high, Fne levels were modest, and Rbp9 remained below the detection limit (Figures 6A and S6). However, Rbp9 proteins were elevated during pupal and adult stages (Figure S6). We confirmed these data using a 3x-myc-tagged Rbp9-BAC genomic transgene. We could barely detect myc-Rbp9 above background in the L1-CNS, while it was abundant in pupal CNS (Figure 6B–C). Thus, Fne seemed more plausible as an overlapping APA factor to Elav during L1, when *elav* mutants are lethal.

We recombined *elav[5]* with the deletion allele *Δfne* (referred to as *elav/fne* double mutants). By removing eggshells, we were able to obtain double mutant L1 larvae, which were highly locomotor defective. We confirmed their genotype by immunostaining, which showed complete absence of Elav and Fne in the appropriate L1 CNS genotypes (Figure 6D–G). Intriguingly, while Elav was nuclear and Fne cytoplasmic in wildtype, Fne localization was altered in *elav* mutants. In particular, Fne was noticeably nuclear in *elav* mutants (Figure 6D–E), and in some regions of *elav* mutant CNS, Fne was predominantly nuclear (Figure 6F). As ELAV/Hu-induced 3’ UTR extensions are mediated during processing of nascent chromatin-associated transcripts, these data suggest that nuclear relocalization of Fne may maintain neural-specific 3’ UTR extensions in *elav* mutants.

Elav represses an unannotated, conserved, alternate splice isoform of Fne that is nuclearly localized

We sought insight into the relocalization of Fne in *elav* mutants. Inspection of the *fne* locus in our RNA-seq data from dissected control (*Canton-S*) and *elav* mutant L1-CNS, revealed three regulatory alterations (Figure 6H). First, *fne* APA is highly sensitive to Elav, as its 3’ UTR extension was nearly entirely lost in *elav* mutants. Second, total *fne* levels were upregulated (1.7-fold) in *elav* mutants. Third, we noticed appearance of an unannotated *fne* exon in *elav* mutant CNS (Figure 6H). While this isoform was not recognized after extensive analysis of the *Drosophila* transcriptome (Brown et al., 2014), it is well-expressed in *elav* mutants and deeply-conserved across insects.

The Fne microexon (which we term 4c), inserts a peptide in the hinge between RRMs 2 and 3, which is relevant for nuclear localization of ELAV/Hu proteins (Fan and Steitz, 1998; Yannoni and White, 1999) (Figure 6I). Interestingly, we found the single ELAV/Hu gene in

Author Manuscript Author Manuscript Author Manuscript Author Manuscript

Apis mellifera (honeybee) is alternatively spliced to include the same microexon (Decio et al., 2019). Given the near identity of these proteins (Figure 6J), we infer that the ancestral ELAV/Hu bee gene is actually an Fne homolog.

To test if the alternate splice isoforms of *Drosophila* Fne are relevant to neural APA, we compared their subcellular localization. As mentioned, when using *actin* promoter constructs (Figures 3–5), all three ELAV/Hu proteins were detected in nucleus and cytoplasm in S2 cells. It is known that ELAV/Hu proteins are shuttling and their localization is influenced by concentration (Zaharieva et al., 2015). Thus, we sought more controlled settings by using *metallothionein* promoter-inducible constructs (Figure 6K). With these reagents, we established conditions where ectopic Elav was predominantly nuclear, while Rbp9 and Fne were predominantly cytoplasmic (Figure 6L–N). By contrast, parallel analysis of Fne-4c showed that it was dominantly nuclear (Figure 6O). This provides strong evidence for a regulatory feedback of ELAV/Hu factors that can compensate neural APA under genetically compromised conditions: loss of *elav* leads to both upregulation and isoform switching of *fne*, which endows it with enhanced capacity for nuclear localization.

Compensatory activities of Elav and Fne direct the neural 3’ UTR extension landscape

The *fne* locus is an example of a highly Elav-dependent neural APA event (Figure 6H), but other presumed Elav-dependent loci were maintained in *elav*-null CNS (Figure 1). To evaluate the activities of Elav and Fne in specifying neural APA, we tested a panel of targets in single and double mutants of these loci. Analysis of universal and extension amplicons of selected neural APA loci from whole L1 larvae showed no loss of 3’ UTR extensions in *fne* mutants alone (Figure S7A), consistent with their overall subtle defects. However, deletion of *fne* strongly enhanced the effects of *elav* mutants for all loci tested. With the exception of *pum*, whose 3’ UTR extension was strongly Elav-dependent, all other loci tested by qPCR exhibited selective loss of extension (but not universal isoforms) only in double mutants (Figure 7A).

These data motivated us to generate 3’-seq and RNA-seq data from *elav/fne* double deletion L1 CNS, to compare with *elav* mutant and wildtype L1 CNS (Table S1). Although these samples are tedious to dissect owing to poor tissue integrity, we emphasize that generation of pure larval CNS from nominally “embryonic lethal” *elav* and even *elav/fne* double mutants offers important advantages. First, this bypasses concerns that these aberrant nervous systems might not develop on schedule during embryogenesis. Second, this minimizes contamination of neural APA changes with universal isoforms expressed throughout non-neural tissues.

Excitingly, the double mutant genotype provided broad evidence for loss of the characteristic neural-extended 3’ UTR landscape. Figure 7B and Figure S7B provide examples of shifts in neural APA in these mutants. As expected, 3’-seq data permits partial isoform shifts to be visualized more clearly than with RNA-seq data alone. Some loci showed substantial effects in *elav* single mutants, but the extent of 3’ UTR shortening was often enhanced in double mutants. However, a striking number of loci exhibited strongly biased shifts towards proximal 3’ UTR isoforms only in *elav/fne* double mutants. We utilized our atlas of tissue and cell 3’-seq data (Sanfilippo et al., 2017b), along with L1-CNS data from this study, to

Author Manuscript Author Manuscript Author Manuscript Author Manuscript

define a manually curated set of 392 genes with neural 3' UTR extension relative to multiple other settings (Table S4). Of these, ~2/3 were genetically dependent on Elav and/or Fne, and most of these loci strongly required both of them (Figure 7C). Therefore, functionally overlapping activities of Elav and Fne are largely responsible for determining the neural 3' UTR extension landscape in the L1 CNS.

We applied our 3' UTR analysis pipelines to these data. We first classified polyA sites, analogous to the S2 analysis, but here using *elav[5]/Δfne* mutants to define dominant universal sites in L1-CNS (Figure 7D). Using these classifications, we determined sequence differences in the vicinity of cleavage sites that were affected in single or double Hu factor mutants. First, we analyzed polyadenylation signals. Universal sites that were preferentially bypassed in wildtype (i.e., by endogenous Elav and Fne) exhibited lower frequencies of optimal PAS (AWUAAA), compared to universal sites in APA genes that were not affected in *elav/fne* double mutants (Figure 7E). In addition, the top *de novo* motifs enriched in 0–50 nt downstream of these bypassed CNS PAS were U-rich motifs that closely matched ELAV/Hu-binding sites (Figure 7F). These motifs were positionally enriched just downstream of PAS and enriched at sites that were subject to Elav/Fne-mediated lengthening (Figure 7G). We obtained qualitatively similar results when comparing *elav[5]* to *Canton-S* L1-CNS, although there the motif enrichment was moderated (Figure S8A), consistent with the milder APA shift in *elav* single mutants. All of these results were very complementary to our ectopic ELAV/Hu studies in S2R+ cells, demonstrating that endogenous Elav and Fne promote neural 3' UTR lengthening genome-wide by preferential association downstream of weaker PAS sites.

To visualize the extent of shifts in the neural APA landscape, we plotted distal 3' UTR usage and weighted 3' UTR lengths between pairwise sets of control *Canton-S* and mutant datasets (Tables S5-6). We observe a highly directional APA shift between *elav[5]* and *Canton- S*, highlighting that 3'-seq data is advantageous for quantifying APA shifts (94 genes with higher distal 3' UTR usage in wildtype L1 CNS, Figure S8B). However, we observed a stronger trend for directional APA shift when comparing *elav[5]* with *elav[5]/Δfne* L1 CNS (117 genes with higher distal 3' UTR usage in *elav[5]*, Figure S8B). This indicates that the normally non-essential factor Fne becomes critical when Elav is deleted. Accordingly, we observe the greatest loss of neural APA when both Elav/Fne are deleted (Figure 7H).

Since neural APA is highly distinct in that it generates extremely long 3' UTRs, we also employed the weighted length metric to visualize large scale changes in overall 3' UTR isoform lengths. These analyses similar show a highly directional trend towards longer 3' UTRs in wildtype CNS compared to either single or double *elav/fne* knockout (Figure 7I and Figure S8C), and emphasizes that scores of loci change by >500bp across the aggregate APA isoforms in *elav[5]/Δfne* double mutants.

Taken together, these results demonstrate overlapping roles of endogenous Elav and Fne for global induction of neural extended 3' UTRs. To our knowledge, this is the first demonstration of trans-acting factors that globally maintain this very distinctive tissue-specific APA landscape.

Author Manuscript Author Manuscript Author Manuscript Author Manuscript

Discussion

Multiple *Drosophila* Hu family RBPs determine the neural extended 3’ UTR landscape

The accumulation of substantially extended 3’ UTR isoforms in the nervous system represents a broad and conserved phenomenon (Hilgers et al., 2011; Miura et al., 2013; Sanfilippo et al., 2017b; Shulman and Elkon, 2019; Smibert et al., 2012; Ulitsky et al., 2012). This phenomenon was associated with activity of Elav (Hilgers et al., 2012; Oktaba et al., 2015), a neuronally-enriched RBP that has been shown to block proximal PAS usage by binding to U-rich sequences (Hilgers et al., 2012; Soller and White, 2003). However, the evidence was limited to a handful of loci. Therefore, the endogenous contribution of Hu RBPs to the general neural 3’ UTR extended landscape, and the mechanism of their regulatory impacts, were largely unknown. Indeed, our initial studies challenged the notion that Elav alone is critical for this process, since analysis of full knockout *elav* larval CNS showed they still broadly express neural 3’ UTR extensions.

We resolve this conundrum with two main lines of evidence. First, we show that a family of neural Hu family RBPs in *Drosophila* all have capacity to broadly induce neural 3’ UTR extensions, largely by promoting the bypass of proximal PAS to permit continued transcription of extension regions. Second, we reveal that there is substantial endogenous functional overlap of the Hu RBPs Elav and Fne in broadly driving endogenous neural 3’ UTR lengthening. Since Fne proteins accumulate modestly in embryos, later timepoints were essential to better reveal their genetic interactions. Although many cells and tissues exhibit characteristic 3’ UTR profiles, the mechanisms are little known. This work reveals the first demonstration of wholesale loss of a tissue-specific APA landscape, here revealed upon co-deletion of *elav* and *fne*.

Many hundreds of genes acquire distinct presumably regulatory capacity as a result of neural APA, which can add miRNA and RBP sites and change overall 3’ UTR structures (Miura et al., 2014). However, until experimental interventions are performed, it is difficult to say how important these extensions are for normal gene regulation, cell behavior, or organismal phenotype. Recently, we used CRISPR engineering to show that neural 3’ UTR extension of *homothorax* contains an array of binding sites for miR-iab-4/8 that control its protein output and are critical for normal adult behavior (Garaulet et al., 2020b). In particular, deletion of the *mir-iab-4/8* locus, surgical mutation of their binding sites in the *homothorax* 3’ UTR, and specific deletion of the *homothorax* neural 3’ UTR extension, all derepress Homothorax in a specific region of the abdominal ventral nerve cord and induce defective virgin female behavior (Garaulet et al., 2020b). Notably, our current data show that the *homothorax* 3’ UTR extension is largely maintained in *elav* mutant CNS, but completely lost in *elav/fne* double mutant CNS (Figure S7B). Thus, ELAV/Hu-RBPs are upstream regulators to this newly-recognized behavioral switch, and their combinatorial activities are presumably relevant to other neural-specific 3’ UTR biology, since they maintain hundreds of neural 3’ UTR extensions.

Author Manuscript Author Manuscript Author Manuscript Author Manuscript

Cross-regulatory and compensatory activities of ELAV/Hu family RBPs

ELAV family proteins have been assigned gene-specific roles in regulating RNA processing at all levels (Mirisis and Carew, 2019), including alternative splicing, APA, target stability, translation, and subcellular mRNA localization (Hilgers et al., 2012; Kraushar et al., 2014; Lee et al., 2012; Lisbin et al., 2001; Peng et al., 1998; Soller and White, 2003; Toba et al., 2002; Zhu et al., 2007). It was initially thought that individual ELAV/Hu family members would adopt distinct RNA processing functions based on cellular localization. Despite a preferred cellular localization, however, they shuttle between the nucleus and the cytoplasm, and localization also depends on cell type (Fan and Steitz, 1998). Accordingly, *Drosophila* Fne and Rbp9 can regulate the Elav targets *ewg*, *nrg* and *arm* (Zaharieva et al., 2015). Such functional overlap was not anticipated as Fne and Rbp9 are normally cytoplasmic (Zaharieva et al., 2015). Our data suggest that modest levels of nuclear ELAV/Hu proteins can promote genomically widespread neural 3' UTR extensions, since Fne comprises a small fraction of total ELAV/Hu proteins in larval CNS. Conversely, while Elav is largely utilized as a nuclear marker, we documented it also has ubiquitous cytoplasmic accumulation (Sanfilippo et al., 2016), so it may conceivably overlap with cytoplasmic Fne/Rbp9 activities.

Complex regulatory interactions amongst the *Drosophila* Hu factors have been documented, since misexpression of Fne results in downregulation of endogenous Elav and Fne (Samson and Chalvet, 2003), and misexpression of a NLS-tagged nuclear variant of Rbp9 results in relocalization of endogenous Elav into the cytoplasm (Zaharieva et al., 2015). We now document multiple additional cross-regulatory mechanisms that control total nuclear levels of ELAV/Hu proteins in *Drosophila*. First, Elav represses *fne* transcript levels, which may be associated with the strong control of *fne* neural 3' UTR extension by Elav. Second Fne represses an alternative splice isoform of Fne that is preferentially localized to the nucleus. This Fne microexon, while not previously annotated, is deeply conserved in insects and may reflect the sole ELAV/Hu protein in other arthropods that is likely to carry out both nuclear and cytoplasmic activities (Samson, 2008). By contrast, even though *Drosophila elav* is the only lethal member of the family, it is intronless and is presumably a derived retrogene copy that originated in the Drosophilid ancestor. The Fne microexon inserts sequence adjacent to the octapeptide in the hinge region, which is known to be involved in nuclear localization. As the hinge region is not sufficient for nuclear localization, other parts of the ELAV/Hu protein may also contribute to its subcellular control (Yannoni and White, 1999).

Cross-over in their regulatory functions is facilitated by the highly overlapping *in vitro* target specificities of ELAV/Hu factors, including Elav/Fne/Rbp9 (Ray et al., 2013). Consistent with this, we find that Elav/Fne/Rbp9-repressed cleavage sites are enriched for similar U-rich motifs. Interestingly, we identified the same motif as a high affinity initiator for forming a larger and saturable megadalton Elav complex (Soller and White, 2005). In addition, the same motif is the main conserved element in *Drosophila virilis* about 100 bp distal of the regulated polyA site in an otherwise very distinct extended binding sequence in *ewg* (Haussmann et al., 2011).

Our data suggest that Rbp9 may also play a role in neural APA, since it has very similar gain-of-function activities as Elav and Fne. However, its impact may be masked by the earlier accumulation of Elav and Fne proteins in neurons. Because of apparent embryonic

Author Manuscript Author Manuscript Author Manuscript Author Manuscript

lethality of available *elav/fne/rbp9* triple mutant genotypes, we could not analyze this genotype at a developmentally relevant post-embryonic timepoint (i.e. in 2nd instar larval CNS when Rbp9 protein is more detectably accumulated). As we suspect that simple RNAi approaches will be insufficient to eliminate the relevant activities, FLP-out systems (Zaharieva et al., 2015) or somatic CRISPR (Port et al., 2020) might be investigated to bypass early lethality of *elav* mutants.

STAR METHODS

RESOURCE AVAILABILITY

Lead Contact. Requests for materials should be directed to and will be fulfilled by the Lead Contact, Eric Lai (laie@mskcc.org).

Materials Availability. All unique reagents generated in this study are available from the Lead Contact with a completed Materials Transfer Agreement. Plasmids generated in this study, all antibodies and used oligodeoxynucleotides are listed in Table S7.

Data and Code Availability. All of the raw RNA-seq and 3'-seq datasets from S2 cells and L1-CNS were deposited in the NCBI Gene Expression Omnibus under GSE155534.

EXPERIMENTAL MODEL AND SUBJECT DETAILS

Drosophila* cell lines—Drosophila melanogaster* S2R+ cells were maintained in Schneider's Insect Medium supplemented with 10% heat inactivated FBS (VWR) and 1% Penicillin-Streptomycin (Thermo Fisher Scientific) at 25 °C. Cells were regularly passaged with the density of 2×10^6/mL. Cell transfection was performed using Effectene (Qiagen) according to the manufacturer's instructions. Transfections were done using cells at <20 passages.

***Drosophila melanogaster* strains—**We used *Canton-S* as a wildtype reference, and the deletion alleles *elav[5]* and *Δfne*. The single *elav* mutant and *elav/fne* double mutants were maintained over *FM7, Dfd-GFP*. Flies were cultured at 25°C under 12:12 LD cycles. To select mutant 1st instar (L1) larvae, heterozygous *elav* or *elav/fne* double mutants were crossed to balancer males, and eggs were collected on an agar plate for 2 hrs. at 25°C. The plates were aged for 22 hrs at 25°C to permit hatching of heterozygote progeny. We collected the embryos in phosphate buffered saline (PBS), treated them with 50% sodium hypochlorite containing 0.1% Triton X-100 for 10 min at 25°C, then washed with PBS twice. This treatment renders the eggshell transparent, facilitating scoring of the Dfd-GFP marker. We then selected individual L1 larvae lacking GFP as homozygous *elav* or *elav/fne* mutants, for total RNA extraction or CNS dissection. Oligonucleotides used for genotyping are listed in Table S7.

METHOD DETAILS

***Drosophila* immunostaining—**We analyzed wt and mutant CNS by dissecting them from 1st instar larvae in cold PBS using Dumont #5 forceps (Fine Science Tools). The CNS were fixed in 4% paraformaldehyde in PBS (Sigma Aldrich) at room temperature for 1 hr,

Author Manuscript Author Manuscript Author Manuscript Author Manuscript

followed by two washes in PBS with 0.2% Tween 20 (PBST), each for 30 min. The following primary antibodies were used: mouse anti-elav (1: 1000; DSHB), and rat anti-Fne (1: 200; gift from Marie Laure Samson). Samples were incubated with the primary antibody for 1 day at 4°C with gentle rotation, followed by two washes in PBST, each 30 min. Secondary antibodies were goat anti-mouse IgG Alexa Fluor 546, and goat anti-rat lgG Alexa Fluor 633 (each 1:1000, Invitrogen). Samples were incubated in secondary antibodies for 1 day at 4°C with gentle rotation, followed by two washes in PBST, each 30 min. Samples were incubated with DAPI in PBS at room temperature for 1 hr before mounting. Imaging was performed on a Leica SP5 spectral confocal microscope using HCX PL APO 63X~/0.70 and HCX PL APO 100X~/1.25–0.75 lenses and processed using FIJI.

Plasmids—We obtained coding sequences of wildtype RNA binding proteins (Elav, Rbp9, Fne, Sxl, Ssx, hnRNPC) by reverse transcription of polyA+ RNA from *Canton-S* heads, and cloned them into pGEM-T vector (Promega). After sequence verification by sanger sequencing, each coding sequence was then sub-cloned into pAc5.1C vector double digested by Xho I and Xba I (except for Fne uses Not I and Xba I sites). Single Flag/HA tags were added at the N-terminus of each coding sequence.

To generate mutant versions of the three Hu family members, we introduced inactivating point mutations into each of the three RNA recognition motifs (RRMs) of Elav, Rbp9 and Fne using site-directed mutagenesis. This yielded pAc5.1C-Elav-RRM3XMT, pAc5.1C-Rbp9-RRM3XMT, pAc5.1C-Fne-RRM3XMT plasmids. Mutations were verified by Sanger sequencing.

To generate the Fne-4C version of Fne recombinant construct, we applied site-directed mutagenesis strategy to split the sequence of 4C exon on both forward and reverse primers, designed to amplify pAc5.1C-Fne to clone pAc5.1C-Fne-4C.

To generate inducible expression constructs of wildtype RNA binding proteins (Elav, Rbp9, Fne, and Fne-4C), we sub-cloned each coding sequence from pAc5.1C vector into pENTR™/D-TOPO™ vector (Invitrogen) using pENTR™/D-TOPO™ cloning kit, generating pENTR-Elav, pENTR-Rbp9, pENTR-Fne, pENTR-Fne-4C, and verified by Sanger sequencing; then, we performed Gateway™ LR cloning (Invitrogen) between each pENTR construct and MT-GAx-CoPuro vector to obtain: MT-GAx-Elav-CoPuro, MT-GAx-Rbp9-CoPuro, MT-GAx-Fne-CoPuro, MT-GAx Fne-4C-CoPuro. All constructs were sequence verified by Sanger sequencing. Oligonucleotides used for cloning are listed in Table S7.

Drosophila* S2R+ cells immunostaining—Drosophila melanogaster* S2R+ cells were transfected with MT-GAx-Elav-CoPuro, MT-GAx-Rbp9-CoPuro, MT-GAx-Fne-CoPuro, MT-GAx Fne-4C-CoPuro according to the protocol mentioned above. A total of 500 ng plasmid was used in each transfection in 12-well plate; 48 hrs. post-transfection, $CuSO_4$ was added to the culture medium at a final concentration of 250 μM to induce recombinant protein expression; 6 hrs. post-induction, harvest cells for immunostaining.

Author Manuscript Author Manuscript Author Manuscript Author Manuscript

Coverslips were treated with 0.01% poly-L-lysine in ddH_2O at 37°C for 1 hr., washed with ddH_2O twice and 70% ethanol once, then dried in the hood under UV light. Cell density was adjusted before loading cells on coverslips, and transferring the plate into 25°C incubator for 2 hrs. Then the media was removed, cells were fixed using 4% PFA in PBS at room temperature for 1 hr. The coverslips were fixed in PBS twice, incubated with PBST (PBS containing 0.1% Triton-X-100) 3 × 3 min., followed by blocking using 10% normal goat serum in PBST at room temperature for 1 hr. with gentle rotation. After blocking, the coverslips were washed with PBST for 5 min, and incubated with primary antibodies. Mouse anti-Lamin C antibody (1:1000, DSHB) was diluted in blocking buffer and incubated with coverslips at 4°C overnight with gentle rotation, followed by 4 washes in PBST, each 15 min. Coverslips were then incubated with secondary antibody goat anti-mouse IgG Alexa Fluor 546 (1:1000, Invitrogen) at room temperature for 2 hrs., followed by 4 washes in PBST, each 15 min. Coverslips were incubated with DAPI in PBS (1:1000, Invitrogen) at room temperature for 1 hr. before mounting. Imaging was performed on a Leica SP5 spectral confocal microscope using HCX PL APO 100X~/1.25–0.75 lenses and processed using FIJI.

RNA extraction, reverse transcription and real-time PCR—We used TRIzol to extract RNAs from S2R+ cells and tissues. To process tissues, ~30–40 whole 1st instar larvae or pools dissected CNS were homogenized in 200 μL TRIzol using a Dounce tissue homogenizer (Thermo Fisher Scientific). L1 CNS dissections were performed in batches, with temporary storage on ice for <30 min before addition of TRIzol and storage at – 80°C. While wildtype L1 CNS can be relatively easily separated from other larval tissues, *elav* and *elav/fne* mutant CNS exhibit poor integrity and are easily fragmented during dissection, which hampers their isolation. On average, each wildtype L1 CNS took ~3 min to dissect but mutant CNS took 2–3 times longer. We pooled ~30–40 dissected CNS to extract total RNA by Trizol for each biological replicate sample. This yielded ~150–200ng total RNA, with typically lower yields for mutant CNS.

All RNAs were TurboDNase (Invitrogen) treated prior to reverse transcription. Poly(A)+ RNAs were enriched using Oligo(dT)25 magnetic beads (NEB) according to manufacturer's instructions. For reverse transcription using RNAs from S2R+ cells, 1 μg total RNA was used as input with a two-step reverse transcription using SuperScript III reverse transcriptase (Invitrogen) with either $oligo(dT)_{18}$ priming or random priming, then 1/20 of RT product was used in a single real-time PCR reaction. For reverse transcription using RNAs from whole 1st stage larvae, 500 ng total RNA was used as input with a two-step reverse transcription with $oligo(dT)_{18}$ priming, then 1/20 of RT product was used in a single real-time PCR reaction. When quantifying APA genes using total RNA extracted from S2R+ cells, raw Ct values were normalized to *rpl32* for data analysis. When quantify APA genes using cell fractionation RNA extracted from S2R+ cells, raw Ct values were normalized to *rpl32* for total and cytoplasmic RNA samples for data analysis, and raw Ct values were normalized to *roX2* for nuclear and chromatin-associated RNA samples for data analysis. When quantifying APA genes using 4sU-labeled RNA extracted from S2R+ cells, raw Ct values were normalized to *roX2* for data analysis. When quantifying APA genes using total RNA from whole 1st instar larvae, raw Ct values were normalized to *rpl14* for data analysis. Oligonucleotides used for gene expression analysis are listed in Table S7.

Author Manuscript Author Manuscript Author Manuscript Author Manuscript

Northern blot—All Northern analyses in this study were performed largely as described(Smibert et al., 2012) with some modifications. Briefly, 15–20 μg total RNA or 1–2 μg poly(A)+ RNAs were resolved on 1.2% agarose gel prepared in BPTE buffer. Transfer was done using 20x SSC and TurboBlotter (GE Healthcare Life Sciences) according to the manufacturer's instructions. After an overnight transfer, wash membrane with 2x SSC, followed by 20 mM Tris-Cl (pH=8.0), crosslink the membrane and bake at 80°C for 1 hr. DNA probes were generated using either asymmetric PCR with ^{32}P-dCTP according to published protocol (Wooddell and Burgess, 1996), or Megaprime DNA labeling kit (GE healthcare Life Sciences) according to manufacture' s instructions. Probes were further purified using Illustra MicroSpin G-25 columns (GE Healthcare Life Sciences). Pre-hybridization (1 hr) and hybridization (overnight) were done using ULTRAhyb™ ultrasensitive hybridization buffer (Invitrogen), at 50°C instead of 42°C to reduce non-specific probe binding. Followed by two non-stringent washes and two stringent washes. Membranes then are exposed to a storage phosphor screen (Thermo Fisher Scientific) for 24–48 hrs at room temperature, then scanned using Typhoon™ FLA 7000 biomolecular imager (GE Healthcare Life Sciences). All Northern blot results were analyzed using Fiji-ImageJ. Oligonucleotides used to generate Northern probes are listed in Table S7.

Cell fractionation and Nascent transcript isolation—72 hrs. post-transfection, S2R+ cells were harvested and washed three times with PBS. Cell fractionation was performed as described (Khodor et al., 2011). Briefly, cells were lysed in hypotonic buffer (15 mM HEPES pH 7.6, 10 mM KCl, 5 mM MgOAC, 3 mM $CaCl_2$, 300 mM Sucrose, 0.1% Triton X-100, 1 mM DTT, 1X complete protease inhibitors) to break the cell membrane and release cell nucleus. Nuclei were purified by centrifugation through sucrose cushion to get rid of intact cells, cell debris etc., then further lysed with nuclear lysis buffer (10mM HEPES-KOH, pH 7.6, 100 mM KCl, 0.1 mM EDTA, 10 % glycerol, 0.15 mM Spermine, 0.5 mM Spermidine, 0.1 M NaF, 0.1 M Na_3VO_4, 0.1 mM $ZnCl_2$, 1 mM DTT, 1X complete protease inhibitors, 1 U/μL SuperaseIn), then 2X NUN buffer (25 mM HEPES-KOH pH 7.6, 300 mM NaCl, 1 M Urea, 1 % NP-40, 1 mM DTT, 1X complete protease inhibitors, 1 U/μL SuperaseIn) was added to the suspension with 1:1 ratio to nuclear lysis buffer. After centrifugation, the supernatant comprises nuclear lysate while the pellet contains DNA/Histones/Pol II-RNA containing nascent RNA transcripts. We saved 5% of each fraction for western blot analysis, and subjected the remainder to RNA extraction using TRIzol or TRIzol LS (Invitrogen).

4sU-labeling and 4sU-containing transcripts isolation—Cells were cultured in medium supplemented with 100 μM of 4sU for 1 hr. before harvest. Total RNA was extracted using TRIzol. 4sU-labeled and pre-existing RNA populations were fractionated using a published method (Radle et al., 2013). Briefly, 100 μg of total RNA was diluted in 1X Biotinylation buffer (100 mM Tris pH 7.4, 10 mM EDTA) with biotin-HPDP (1 μg/μl in DMF), incubated at room temperature on a rotator for 1.5 hrs. RNA was then extracted with Phenol: Chloroform: Isoamyl Alcohol and precipitated in EtOH for at least 2 hrs. RNA pellet was dissolved in 50 μl of nuclease-free H_2O and denatured by incubation at 70 °C for 2 min. After chilling on ice, RNA was mixed with 50 μl of pre-washed Streptavidin C1 Dynabeads in 2X bind and wash buffer (10 mM Tris-HCl pH 7.5, 1 mM EDTA, 2 M NaCl, 1

Author Manuscript Author Manuscript Author Manuscript Author Manuscript

U/μl SuperaseIn). Mixture was incubated on a rotator at room temperature for 1 hr. After incubation, collecting beads on a magnetic stand, discard the supernatant containing the pre-existing RNAs; wash the beads three times with 0.5 ml of 1x bind and wash buffer (5 mM Tris-HCl pH 7.5, 0.5 mM EDTA, 1 M NaCl) at 65 °C, followed by three washes with 1X bind and wash buffer at room temperature. After complete removal of the bind and wash buffer, resuspend the beads with 200 μl of 1x bind and wash buffer containing 100 mM DTT, incubated at room temperature for 3 min to elute 4sU-labeled RNA. The elution process was repeated one more time and the eluted RNA was precipitated as described above. The isolated RNA was used for RT-qPCR.

3'-end sequencing libraries and mapping—3'-end sequencing libraries of cell line RNA samples were prepared using a custom method as described (Sanfilippo et al., 2017a). Briefly, 3'-end sequencing libraries were prepared using 2 mg of total RNA as starting material. Total RNA was chemically fragmented and custom oligo(dT) primers were used to capture and synthesize cDNAs representing junctions of 3'-end of transcripts and poly(A) tails. As far less material was available for dissected L1-CNS RNA samples, we prepared these 3'-end sequencing libraries using QuantSeq 3' mRNA-seq library preparation REV kit for Illumina (Lexogen) with a starting material of 50 ng total RNA, according to manufacturer's instructions. cDNA libraries were sequenced on Illumina HiSeq-1000 sequencer with SE-50 mode. Data were mapped onto the corresponding UCSC genome assemblies: *Drosophila melanogaster* (dm6) and 3′ end clusters were derived and quantified within a 25 bp window as described (Sanfilippo et al., 2017a).

RNA-seq libraries and mapping—Total RNA-seq libraries were prepared using TruSeq Stranded Total RNA Library Preparation Kit (Illumina) with either 0.1 μg input RNA (for 1st instar larval CNS) or 2 μg input RNA (for cells) as starting materials. Final cDNA libraries were sequenced on Illumina HiSeq-1000 sequencer with PE-100 mode. Total RNA-seq data were mapped to the corresponding UCSC genome assemblies: *Drosophila melanogaster* (dm6), HISAT2 aligner was used for the alignment with default parameters (Kim et al., 2015).

Gene expression analysis—The read counts of either RNA-seq or 3'-seq were normalized by computing the base mean value to receive the expression levels. Differential expression of the genes was analyzed using the DESeq2 R package in Bioconductor (Love et al., 2014).

Analysis of differential 3' UTR isoform expression—For this and all 3'-seq analysis, we only considered CPM>5 3'-seq clusters. To analyze the average length of various 3' UTR isoforms, we calculated the weighted 3' UTR length by normalize the 3'-seq expression and 3' UTR length of each isoform as the total 3'-seq expression of given gene (Sanfilippo et al., 2017b). We defined genes having differential average 3' UTR length greater than 100 bp between two samples as APA gene.

In order to measure the quantitative use of distal isoform, we calculated the expression rate of the isoform expressed downstream than the isoform used predominantly in the control

Author Manuscript Author Manuscript Author Manuscript Author Manuscript

sample. A gene in which the expression of distal isoform differs by more than 20% between two samples was defined as an APA gene.

Analysis of relative strengths of 3' ends—We calculate bypass scores for each 3'-ends by percentage of 3-seq reads downstream of a given 3' end. The bypass ratio was calculated by comparing the bypass score of each 3'-end between two samples in order to compare relative strength of 3' ends. The terminal site without downstream isoform was omitted. Bypass ratio 1 means that a specific 3' end has as much downstream isoforms compared to the control and a ratio 0 means that the total amount of downstream isoform is not changed in both samples. Conversely, the unbypassed ratio is a measure of how much the pA site of a specific sample is not bypassed compared to the control. Maximum strength of unbypassed ratio 1 signifies that no isoforms are detected beyond that site.

Motif analysis—To search for *de novo* motifs around cleavage sites, 50-nucleotide windows downstream of the cleavage site were used for motif discovery analysis using MEME-suite (v 5.0.2) with default parameters (Bailey et al., 2015). Position weight matrix (PWM) of given motifs was analyzed by seqPattern R package in Bioconductor. To plot enrichments of ELAV/Hu motifs relative to cleavage sites (Figure 5G–I), we set aside the termini of the ~1% of genes that appeared to undergo shortening in the presence of Elav/Fne/Rbp9 (Figure 3C–E), as well as extension-terminal sites, which by definition cannot be bypassed (Figure 5A).

QUANTIFICATION AND STATISTICAL ANALYSIS

GraphPad Prism 7 was used for statistical analysis. Statistical parameters including the exact values of n (number of experiments), average and standard deviations of all RT-qPCR results are shown as mean ± SD; and reported in the Figures and corresponding Figure Legends of Figure 1B, Figure 2D, Figure 4C, Figure 4D, Figure 4E, Figure 7A; Figure S2, Figure S4, Figure S5, Figure S7A.

Supplementary Material

Refer to Web version on PubMed Central for supplementary material.

Acknowledgments

We thank Alexandra Panzarino for initial analysis of *elav[5]* larvae and Albertomaria Moro for preliminary inspection of S2 cell 3'-seq data. Work in E.C.L.'s group was supported by the National Institutes of Health (R01-NS083833 and R01-GM083300) and MSK Core Grant P30-CA008748.

References

An JJ, Gharami K, Liao GY, Woo NH, Lau AG, Vanevski F, Torre ER, Jones KR, Feng Y, Lu B, et al. (2008). Distinct role of long 3' UTR BDNF mRNA in spine morphology and synaptic plasticity in hippocampal neurons. Cell 134, 175–187. [PubMed: 18614020]

Bailey TL, Johnson J, Grant CE, and Noble WS (2015). The MEME Suite. Nucleic acids research 43, W39–49. [PubMed: 25953851]

Batra R, Charizanis K, Manchanda M, Mohan A, Li M, Finn DJ, Goodwin M, Zhang C, Sobczak K, Thornton CA, et al. (2014). Loss of MBNL leads to disruption of developmentally regulated

Author Manuscript Author Manuscript Author Manuscript Author Manuscript

alternative polyadenylation in RNA-mediated disease. Molecular cell 56, 311–322. [PubMed: 25263597]

Berg MG, Singh LN, Younis I, Liu Q, Pinto AM, Kaida D, Zhang Z, Cho S, Sherrill-Mix S, Wan L, et al. (2012). U1 snRNP determines mRNA length and regulates isoform expression. Cell 150, 53–64. [PubMed: 22770214]

Berkovits BD, and Mayr C (2015). Alternative 3' UTRs act as scaffolds to regulate membrane protein localization. Nature 522, 363–367. [PubMed: 25896326]

Blair JD, Hockemeyer D, Doudna JA, Bateup HS, and Floor SN (2017). Widespread Translational Remodeling during Human Neuronal Differentiation. Cell reports 21, 2005–2016. [PubMed: 29141229]

Brown JB, Boley N, Eisman R, May GE, Stoiber MH, Duff MO, Booth BW, Wen J, Park S, Suzuki AM, et al. (2014). Diversity and dynamics of the Drosophila transcriptome. Nature 512, 393–399. [PubMed: 24670639]

Calvo O, and Manley JL (2001). Evolutionarily conserved interaction between CstF-64 and PC4 links transcription, polyadenylation, and termination. Molecular cell 7, 1013–1023. [PubMed: 11389848]

Campos AR, Grossman D, and White K (1985). Mutant alleles at the locus elav in Drosophila melanogaster lead to nervous system defects. A developmental-genetic analysis. Journal of neurogenetics 2, 197–218. [PubMed: 3926976]

Casas-Vila N, Bluhm A, Sayols S, Dinges N, Dejung M, Altenhein T, Kappei D, Altenhein B, Roignant JY, and Butter F (2017). The developmental proteome of Drosophila melanogaster. Genome research 27, 1273–1285. [PubMed: 28381612]

Chatrikhi R, Mallory MJ, Gazzara MR, Agosto LM, Zhu WS, Litterman AJ, Ansel KM, and Lynch KW (2019). RNA Binding Protein CELF2 Regulates Signal-Induced Alternative Polyadenylation by Competing with Enhancers of the Polyadenylation Machinery. Cell reports 28, 2795–2806 e2793. [PubMed: 31509743]

Dai W, Zhang G, and Makeyev EV (2012). RNA-binding protein HuR autoregulates its expression by promoting alternative polyadenylation site usage. Nucleic acids research 40, 787–800. [PubMed: 21948791]

Dantonel JC, Murthy KG, Manley JL, and Tora L (1997). Transcription factor TFIID recruits factor CPSF for formation of 3' end of mRNA. Nature 389, 399–402. [PubMed: 9311784]

Decio P, Ustaoglu P, Roat TC, Malaspina O, Devaud JM, Stoger R, and Soller M (2019). Acute thiamethoxam toxicity in honeybees is not enhanced by common fungicide and herbicide and lacks stress-induced changes in mRNA splicing. Scientific reports 9, 19196. [PubMed: 31844097]

Fan XC, and Steitz JA (1998). HNS, a nuclear-cytoplasmic shuttling sequence in HuR. Proceedings of the National Academy of Sciences of the United States of America 95, 15293–15298. [PubMed: 9860962]

Fischl H, Neve J, Wang Z, Patel R, Louey A, Tian B, and Furger A (2019). hnRNPC regulates cancer-specific alternative cleavage and polyadenylation profiles. Nucleic acids research 47, 7580–7591. [PubMed: 31147722]

Franke A, and Baker BS (1999). The rox1 and rox2 RNAs are essential components of the compensasome, which mediates dosage compensation in Drosophila. Molecular cell 4, 117–122. [PubMed: 10445033]

Garaulet DL, Zhang B, Wei L, Li E, and Lai EC (2020a). miRNAs and Neural Alternative Polyadenylation Specify the Virgin Behavioral State. Developmental cell 54, 410–423. [PubMed: 32579967]

Garaulet DL, Zhang B, Wei L, Li E, and Lai EC (2020b). A post-transcriptional regulatory circuit specifies the virgin behavioral state. Developmental cell *in press*.

Gawande B, Robida MD, Rahn A, and Singh R (2006). Drosophila Sex-lethal protein mediates polyadenylation switching in the female germline. The EMBO journal 25, 1263–1272. [PubMed: 16511567]

Gruber AJ, Schmidt R, Gruber AR, Martin G, Ghosh S, Belmadani M, Keller W, and Zavolan M (2016). A comprehensive analysis of 3' end sequencing data sets reveals novel polyadenylation signals and the repressive role of heterogeneous ribonucleoprotein C on cleavage and polyadenylation. Genome research 26, 1145–1159. [PubMed: 27382025]

Author Manuscript Author Manuscript Author Manuscript Author Manuscript

Gruber AJ, and Zavolan M (2019). Alternative cleavage and polyadenylation in health and disease. Nature reviews. Genetics.

Gunderson SI, Polycarpou-Schwarz M, and Mattaj IW (1998). U1 snRNP inhibits pre-mRNA polyadenylation through a direct interaction between U1 70K and poly(A) polymerase. Molecular cell 1, 255–264. [PubMed: 9659922]

Haussmann IU, Li M, and Soller M (2011). ELAV-mediated 3'-end processing of ewg transcripts is evolutionarily conserved despite sequence degeneration of the ELAV-binding site. Genetics 189, 97–107. [PubMed: 21705751]

Hilgers V, Lemke SB, and Levine M (2012). ELAV mediates 3' UTR extension in the Drosophila nervous system. Genes & development 26, 2259–2264. [PubMed: 23019123]

Hilgers V, Perry MW, Hendrix D, Stark A, Levine M, and Haley B (2011). Neural-specific elongation of 3' UTRs during Drosophila development. Proceedings of the National Academy of Sciences of the United States of America 108, 15864–15869. [PubMed: 21896737]

Jenal M, Elkon R, Loayza-Puch F, van Haaften G, Kuhn U, Menzies FM, Vrielink JA, Bos AJ, Drost J, Rooijers K, et al. (2012). The poly(a)-binding protein nuclear 1 suppresses alternative cleavage and polyadenylation sites. Cell 149, 538–553. [PubMed: 22502866]

Ji Z, Luo W, Li W, Hoque M, Pan Z, Zhao Y, and Tian B (2011). Transcriptional activity regulates alternative cleavage and polyadenylation. Molecular systems biology 7, 534. [PubMed: 21952137]

Kelley RL, Meller VH, Gordadze PR, Roman G, Davis RL, and Kuroda MI (1999). Epigenetic spreading of the Drosophila dosage compensation complex from roX RNA genes into flanking chromatin. Cell 98, 513–522. [PubMed: 10481915]

Khodor YL, Rodriguez J, Abruzzi KC, Tang CH, Marr MT 2nd, and Rosbash M (2011). Nascent-seq indicates widespread cotranscriptional pre-mRNA splicing in Drosophila. Genes & development 25, 2502–2512. [PubMed: 22156210]

Kim D, Langmead B, and Salzberg SL (2015). HISAT: a fast spliced aligner with low memory requirements. Nature methods 12, 357–360. [PubMed: 25751142]

Kim YJ, and Baker BS (1993). The *Drosophila* gene *rbp9* encodes a protein that is a member of a conserved group of putative RNA binding proteins that are nervous system-specific in both flies and humans. J. Neurosci 13, 1045–1056. [PubMed: 7680064]

Kim-Ha J, Kim J, and Kim YJ (1999). Requirement of RBP9, a Drosophila Hu homolog, for regulation of cystocyte differentiation and oocyte determination during oogenesis. Molecular and cellular biology 19, 2505–2514. [PubMed: 10082516]

Kraushar ML, Thompson K, Wijeratne HR, Viljetic B, Sakers K, Marson JW, Kontoyiannis DL, Buyske S, Hart RP, and Rasin MR (2014). Temporally defined neocortical translation and polysome assembly are determined by the RNA-binding protein Hu antigen R. Proceedings of the National Academy of Sciences of the United States of America 111, E3815–3824. [PubMed: 25157170]

Kuklin EA, Alkins S, Bakthavachalu B, Genco MC, Sudhakaran I, Raghavan KV, Ramaswami M, and Griffith LC (2017). The Long 3'UTR mRNA of CaMKII Is Essential for Translation-Dependent Plasticity of Spontaneous Release in Drosophila melanogaster. The Journal of neuroscience : the official journal of the Society for Neuroscience 37, 10554–10566.

Lackford B, Yao C, Charles GM, Weng L, Zheng X, Choi EA, Xie X, Wan J, Xing Y, Freudenberg JM, et al. (2014). Fip1 regulates mRNA alternative polyadenylation to promote stem cell self-renewal. The EMBO journal 33, 878–889. [PubMed: 24596251]

Lee EK, Kim W, Tominaga K, Martindale JL, Yang X, Subaran SS, Carlson OD, Mercken EM, Kulkarni RN, Akamatsu W, et al. (2012). RNA-binding protein HuD controls insulin translation. Molecular cell 45, 826–835. [PubMed: 22387028]

Lianoglou S, Garg V, Yang JL, Leslie CS, and Mayr C (2013). Ubiquitously transcribed genes use alternative polyadenylation to achieve tissue-specific expression. Genes & development 27, 2380–2396. [PubMed: 24145798]

Lisbin MJ, Qiu J, and White K (2001). The neuron-specific RNA-binding protein ELAV regulates neuroglian alternative splicing in neurons and binds directly to its pre-mRNA. Genes & development 15, 2546–2561. [PubMed: 11581160]

Author Manuscript Author Manuscript Author Manuscript Author Manuscript

Love MI, Huber W, and Anders S (2014). Moderated estimation of fold change and dispersion for RNA-seq data with DESeq2. Genome biology 15, 550. [PubMed: 25516281]

Mansfield KD, and Keene JD (2012). Neuron-specific ELAV/Hu proteins suppress HuR mRNA during neuronal differentiation by alternative polyadenylation. Nucleic acids research 40, 2734–2746. [PubMed: 22139917]

Masamha CP, and Wagner EJ (2018). The contribution of alternative polyadenylation to the cancer phenotype. Carcinogenesis 39, 2–10. [PubMed: 28968750]

Mirisis AA, and Carew TJ (2019). The ELAV family of RNA-binding proteins in synaptic plasticity and long-term memory. Neurobiol Learn Mem 161, 143–148. [PubMed: 30998973]

Miura P, Sanfilippo P, Shenker S, and Lai EC (2014). Alternative polyadenylation in the nervous system: to what lengths will 3' UTR extensions take us? BioEssays 36, 766–777. [PubMed: 24903459]

Miura P, Shenker S, Andreu-Agullo C, Westholm JO, and Lai EC (2013). Widespread and extensive lengthening of 3' UTRs in the mammalian brain. Genome research 23, 812–825. [PubMed: 23520388]

Oktaba K, Zhang W, Lotz TS, Jun DJ, Lemke SB, Ng SP, Esposito E, Levine M, and Hilgers V (2015). ELAV links paused Pol II to alternative polyadenylation in the Drosophila nervous system. Molecular cell 57, 341–348. [PubMed: 25544561]

Peng SS, Chen CY, Xu N, and Shyu AB (1998). RNA stabilization by the AU-rich element binding protein, HuR, an ELAV protein. The EMBO journal 17, 3461–3470. [PubMed: 9628881]

Pinto PA, Henriques T, Freitas MO, Martins T, Domingues RG, Wyrzykowska PS, Coelho PA, Carmo AM, Sunkel CE, Proudfoot NJ, et al. (2011). RNA polymerase II kinetics in polo polyadenylation signal selection. The EMBO journal 30, 2431–2444. [PubMed: 21602789]

Port F, Strein C, Stricker M, Rauscher B, Heigwer F, Zhou J, Beyersdorffer C, Frei J, Hess A, Kern K, et al. (2020). A large-scale resource for tissue-specific CRISPR mutagenesis in Drosophila. eLife 9.

Radle B, Rutkowski AJ, Ruzsics Z, Friedel CC, Koszinowski UH, and Dolken L (2013). Metabolic labeling of newly transcribed RNA for high resolution gene expression profiling of RNA synthesis, processing and decay in cell culture. Journal of visualized experiments : JoVE.

Ray D, Kazan H, Cook KB, Weirauch MT, Najafabadi HS, Li X, Gueroussov S, Albu M, Zheng H, Yang A, et al. (2013). A compendium of RNA-binding motifs for decoding gene regulation. Nature 499, 172–177. [PubMed: 23846655]

Robinow S, and White K (1991). Characterization and spatial distribution of the ELAV protein during Drosophila melanogaster development. Journal of neurobiology 22, 443–461. [PubMed: 1716300]

Samson ML (2008). Rapid functional diversification in the structurally conserved ELAV family of neuronal RNA binding proteins. BMC genomics 9, 392. [PubMed: 18715504]

Samson ML, and Chalvet F (2003). found in neurons, a third member of the Drosophila elav gene family, encodes a neuronal protein and interacts with elav. Mechanisms of development 120, 373–383. [PubMed: 12591606]

Sanfilippo P, Miura P, and Lai EC (2017a). Genome-wide profiling of the 3' ends of polyadenylated RNAs. Methods 126, 86–94. [PubMed: 28602807]

Sanfilippo P, Smibert P, Duan H, and Lai EC (2016). Neural specificity of the RNA-binding protein Elav is achieved by post-transcriptional repression in non-neural tissues. Development 143, 4474–4485. [PubMed: 27802174]

Sanfilippo P, Wen J, and Lai EC (2017b). Landscape and evolution of tissue-specific alternative polyadenylation across Drosophila species. Genome biology 18, 229. [PubMed: 29191225]

Shulman ED, and Elkon R (2019). Cell-type-specific analysis of alternative polyadenylation using single-cell transcriptomics data. Nucleic acids research 47, 10027–10039. [PubMed: 31501864]

Smibert P, Miura P, Westholm JO, Shenker S, May G, Duff MO, Zhang D, Eads B, Carlson J, Brown JB, et al. (2012). Global patterns of tissue-specific alternative polyadenylation in Drosophila. Cell reports 1, 277–289. [PubMed: 22685694]

Soller M, and White K (2003). ELAV inhibits 3'-end processing to promote neural splicing of ewg pre-mRNA. Genes & development 17, 2526–2538. [PubMed: 14522950]

Soller M, and White K (2004). Elav. Curr Biol 14, R53. [PubMed: 14738746]

Author Manuscript Author Manuscript Author Manuscript Author Manuscript

Soller M, and White K (2005). ELAV multimerizes on conserved AU4–6 motifs important for ewg splicing regulation. Molecular and cellular biology 25, 7580–7591. [PubMed: 16107705]

Takagaki Y, Seipelt RL, Peterson ML, and Manley JL (1996). The polyadenylation factor CstF-64 regulates alternative processing of IgM heavy chain pre-mRNA during B cell differentiation. Cell 87, 941–952. [PubMed: 8945520]

Tian B, Hu J, Zhang H, and Lutz CS (2005). A large-scale analysis of mRNA polyadenylation of human and mouse genes. Nucleic acids research 33, 201–212. [PubMed: 15647503]

Tian B, and Manley JL (2017). Alternative polyadenylation of mRNA precursors. Nature reviews. Molecular cell biology 18, 18–30. [PubMed: 27677860]

Toba G, Qui J, Koushika SP, and White K (2002). Ectopic expression of Drosophila ELAV and human HuD in Drosophila wing disc cells reveals functional distinctions and similarities. Journal of cell science 115, 2413–2421. [PubMed: 12006625]

Ulitsky I, Shkumatava A, Jan CH, Subtelny AO, Koppstein D, Bell GW, Sive H, and Bartel DP (2012). Extensive alternative polyadenylation during zebrafish development. Genome research 22, 2054–2066. [PubMed: 22722342]

Wooddell CI, and Burgess RR (1996). Use of asymmetric PCR to generate long primers and single-stranded DNA for incorporating cross-linking analogs into specific sites in a DNA probe. Genome research 6, 886–892. [PubMed: 8889557]

Yang SW, Li L, Connelly JP, Porter SN, Kodali K, Gan H, Park JM, Tacer KF, Tillman H, Peng J, et al. (2020). A Cancer-Specific Ubiquitin Ligase Drives mRNA Alternative Polyadenylation by Ubiquitinating the mRNA 3' End Processing Complex. Molecular cell 77, 1206–1221 e1207. [PubMed: 31980388]

Yannoni YM, and White K (1999). Domain necessary for Drosophila ELAV nuclear localization: function requires nuclear ELAV. Journal of cell science 112 (Pt 24), 4501–4512. [PubMed: 10574700]

Yao C, Biesinger J, Wan J, Weng L, Xing Y, Xie X, and Shi Y (2012). Transcriptome-wide analyses of CstF64-RNA interactions in global regulation of mRNA alternative polyadenylation. Proceedings of the National Academy of Sciences of the United States of America 109, 18773–18778. [PubMed: 23112178]

Yudin D, Hanz S, Yoo S, Iavnilovitch E, Willis D, Gradus T, Vuppalanchi D, Segal-Ruder Y, Ben-Yaakov K, Hieda M, et al. (2008). Localized regulation of axonal RanGTPase controls retrograde injury signaling in peripheral nerve. Neuron 59, 241–252. [PubMed: 18667152]

Zaharieva E, Haussmann IU, Brauer U, and Soller M (2015). Concentration and Localization of Coexpressed ELAV/Hu Proteins Control Specificity of mRNA Processing. Molecular and cellular biology 35, 3104–3115. [PubMed: 26124284]

Zanini D, Jallon JM, Rabinow L, and Samson ML (2012). Deletion of the Drosophila neuronal gene found in neurons disrupts brain anatomy and male courtship. Genes, brain, and behavior 11, 819–827.

Zhang H, Lee JY, and Tian B (2005). Biased alternative polyadenylation in human tissues. Genome biology 6, R100. [PubMed: 16356263]

Zhang Z, So K, Peterson R, Bauer M, Ng H, Zhang Y, Kim JH, Kidd T, and Miura P (2019). Elav-Mediated Exon Skipping and Alternative Polyadenylation of the Dscam1 Gene Are Required for Axon Outgrowth. Cell reports 27, 3808–3817 e3807. [PubMed: 31242415]

Zhu H, Zhou HL, Hasman RA, and Lou H (2007). Hu proteins regulate polyadenylation by blocking sites containing U-rich sequences. The Journal of biological chemistry 282, 2203–2210. [PubMed: 17127772]

Zhu Y, Wang X, Forouzmand E, Jeong J, Qiao F, Sowd GA, Engelman AN, Xie X, Hertel KJ, and Shi Y (2018). Molecular Mechanisms for CFIm-Mediated Regulation of mRNA Alternative Polyadenylation. Molecular cell 69, 62–74 e64. [PubMed: 29276085]

Author Manuscript Author Manuscript Author Manuscript Author Manuscript

Highlights:

1. Ectopic ELAV/Hu RBPs (Elav/Rbp9/Fne) induces global neural 3’ UTR extensions
2. ELAV/Hu RBPs mediate bypass of proximal pA signals at the nascent transcript level
3. *elav* mutants induce an *fne* splicing switch to relocalize it from cytoplasm to nucleus
4. *elav*/*fne* double mutant larval CNS exhibit dramatic loss of neural 3’ UTR extensions

Author Manuscript Author Manuscript Author Manuscript Author Manuscript

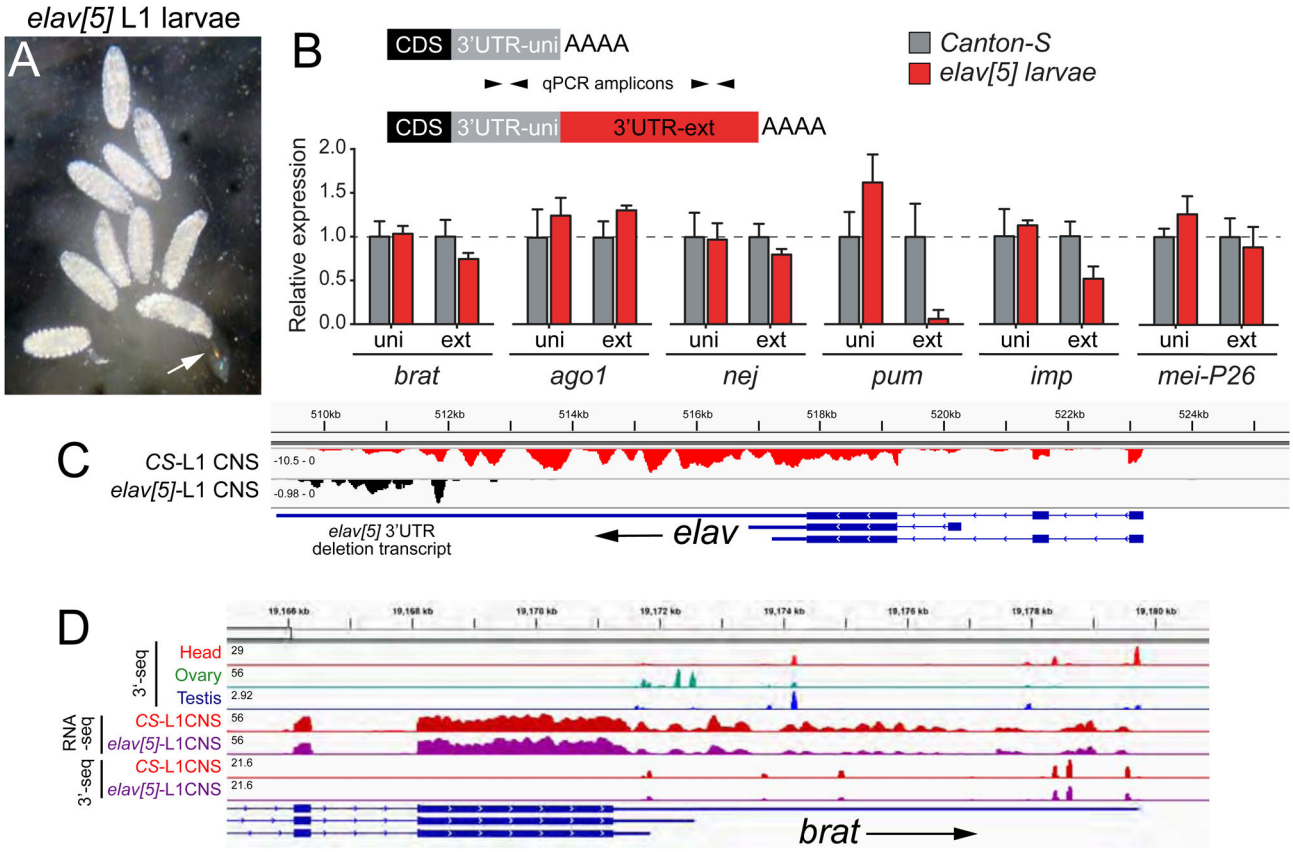

Figure 1. Elav is not essential for the accumulation of neural 3' UTR extensions

(A) Brightfield image of viable homozygous *elav[5]* deletion 1st instar (L1) larvae after removal of eggshells (see arrow). (B) qRT-PCR analysis of universal (uni) and extension (ext) 3' UTR amplicons of genes previously reported to harbor fully Elav-dependent neural 3' UTR extension isoforms (Hilgers et al., 2011). With the exception of *pumilio* (*pum*), these genes accumulated 3' UTR extensions in *elav[5]* L1 as in control *Canton-S* L1 larvae; *imp* showed partial dependence. Relative expression level was calculated by normalizing raw Ct values to *rpl14*, error-bar represents standard deviation (mean ± SD; n = 3). (C) Integrated Genome Viewer (IGV) screenshots of RNA-seq data from hand-dissected CNS from *Canton-S* and *elav[5]* L1 larvae. Elav locus shows complete absence of coding and most UTR signals from *elav[5]* deletion larvae, verifying the purity of the mutant selection. A mutant transcript containing the very distal portion of *elav* 3' UTR extension is present in *elav[5]*. Note that the range scaling of this track is >10x that of the wildtype reference, so this is a minor transcript. (D) Example of a prominent neural 3' UTR extension that is still expressed in *elav[5]* L1 CNS. See also Figure S1.

Author Manuscript Author Manuscript Author Manuscript Author Manuscript

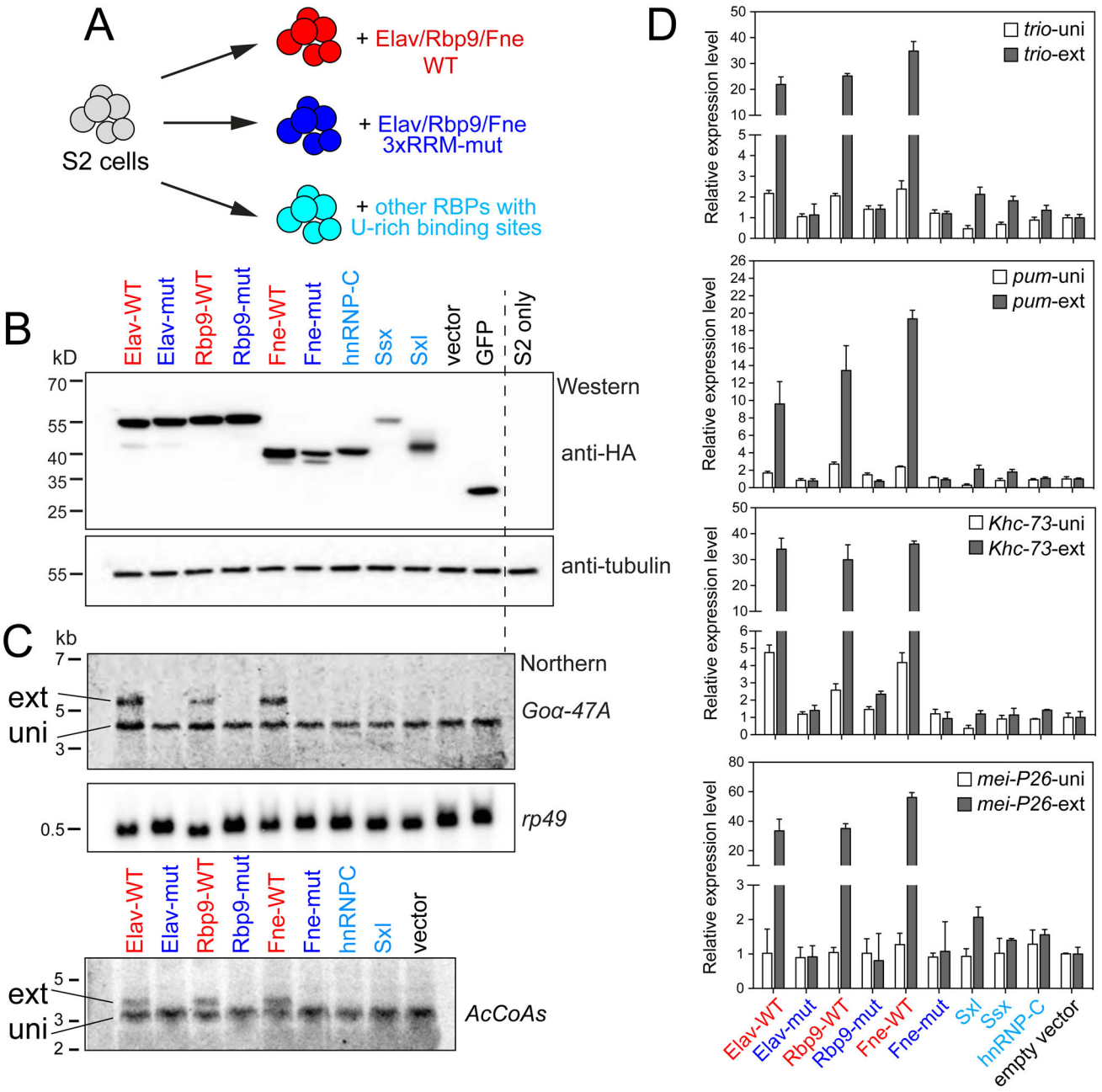

Figure 2. Ectopic Elav/Rbp9/Fne induces neural-specific 3' UTR isoforms in S2R+ cells

(A) Experimental scheme. S2R+ cells were transfected with wildtype ELAV/Hu factors (Elav, Rbp9 and Fne, in red), corresponding variants bearing point mutations in all 3 RRM domains that abrogate RNA-binding activity (blue), or other U-rich RNA binding proteins (aqua). (B) Western blot detecting the tagged proteins, showing that RRM mutations do not compromise accumulation of ELAV/Hu proteins. (C) Northern blotting of cells transfected with the indicated constructs. Wildtype Elav/Rbp9/Fne all specifically induce the accumulation of extended 3' UTR isoforms. Mutant ELAV/Hu proteins or other RBPs with related U-rich binding sequences do not induce these 3' UTR isoforms. (D) qRT-PCR analysis of universal 3' UTR isoforms (uni) and extended 3' UTR isoforms (ext) of

Author Manuscript Author Manuscript Author Manuscript Author Manuscript

additional neural APA genes confirms specific induction of 3’ UTR extensions only by wildtype ELAV/Hu factors. Relative expression level was calculated by normalizing to *rp49* (mean ± SD, n = 3). See also Figure S2.

Author Manuscript Author Manuscript Author Manuscript Author Manuscript

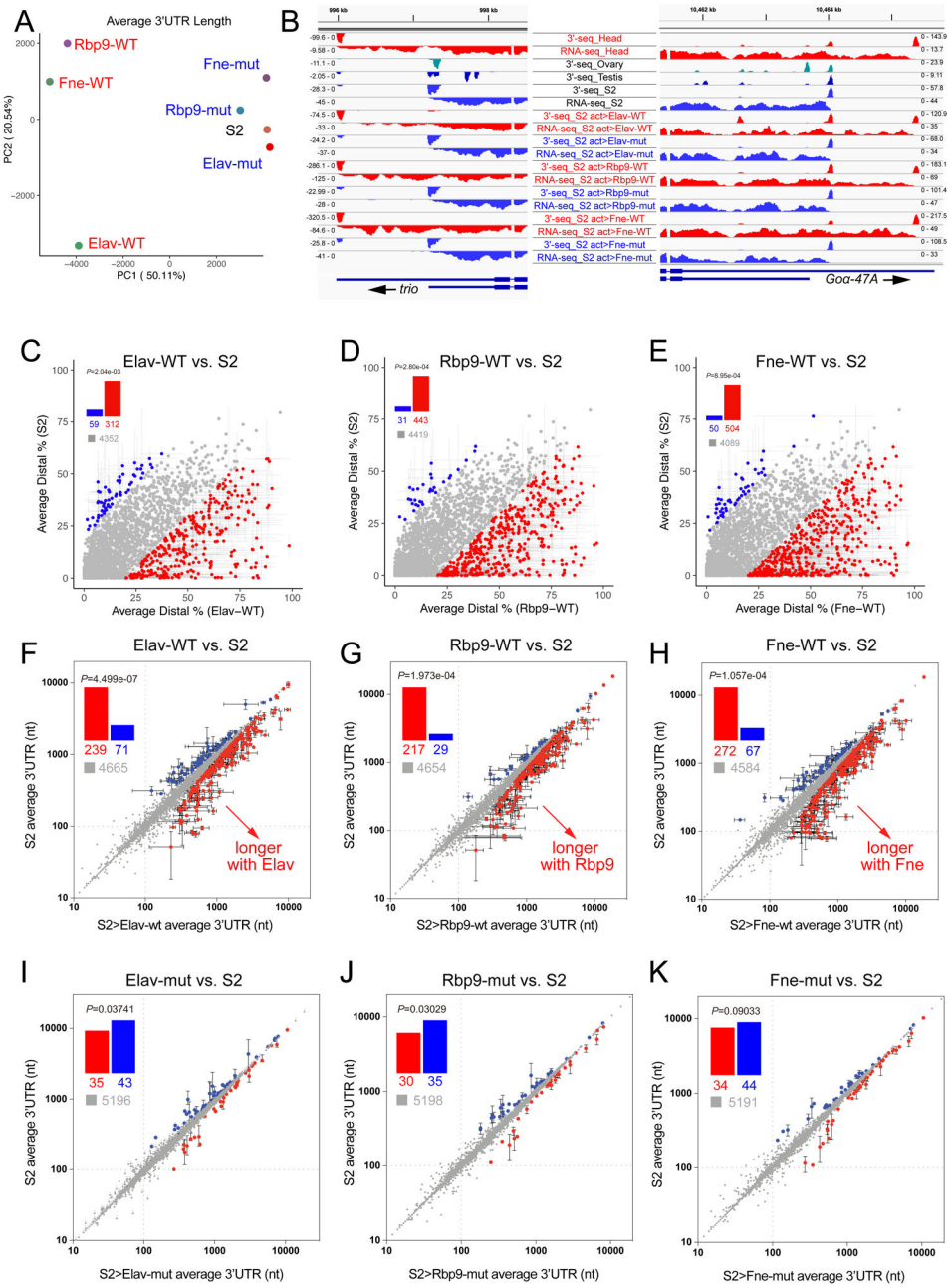

Figure 3. Ectopic Elav/Rbp9/Fne globally induce neural 3’ UTR lengthening in S2R+ cells.

(A) PCA analysis of 3’ UTR lengths in S2R+ cells transfected with wildtype (in red) or 3xRRM-mut (in blue) versions of Elav/Rbp9/Fne. (B) Read coverage tracks of RNA-seq and 3’-seq data tracks illustrating how ectopic expression of all three ELAV/Hu factors induces the accumulation of extended 3’ UTR isoforms that match the neural-specific extended isoform (i.e., in heads). (C-E) Analyses of 3’-seq data to quantify distal 3’ UTR usage, comparing overexpression of Elav (C), Rbp9 (D) and Fne (E) to control S2 cells. Genes exhibiting >20% distal usage change were colored red or blue, depending on the condition of preferred usage. All three ELAV/Hu factors induce broad shifts towards extended isoform usage (red dots). The directionality towards 3’ UTR lengthening is highly significant in all

Author Manuscript Author Manuscript Author Manuscript Author Manuscript

cases (see insets). (F-K) Analysis of weighted 3’ UTR lengths in cells expressing wildtype (F-H) or 3xRRM-mutant (I-K) versions of ELAV/Hu factors. The weighted length metric emphasizes a different aspect of APA deployment than does distal 3’ UTR usage, namely largescale differences in 3’ UTR isoforms; i.e. genes do not have to exhibit substantially different 3’ UTR lengths to score with highly differential distal 3’ UTR usage. Genes showing differential weighted length ≥100 nt at a false discovery rate (FDR) of ≤ 0.05 are colored red or blue, depending on the condition of preferred usage. These analyses show that wildtype ELAV/Hu factors induce large directional changes towards 3’ UTR lengthening, while their RNA binding-defective counterparts induce minimal effects. See also Figure S3.

Author Manuscript Author Manuscript Author Manuscript Author Manuscript

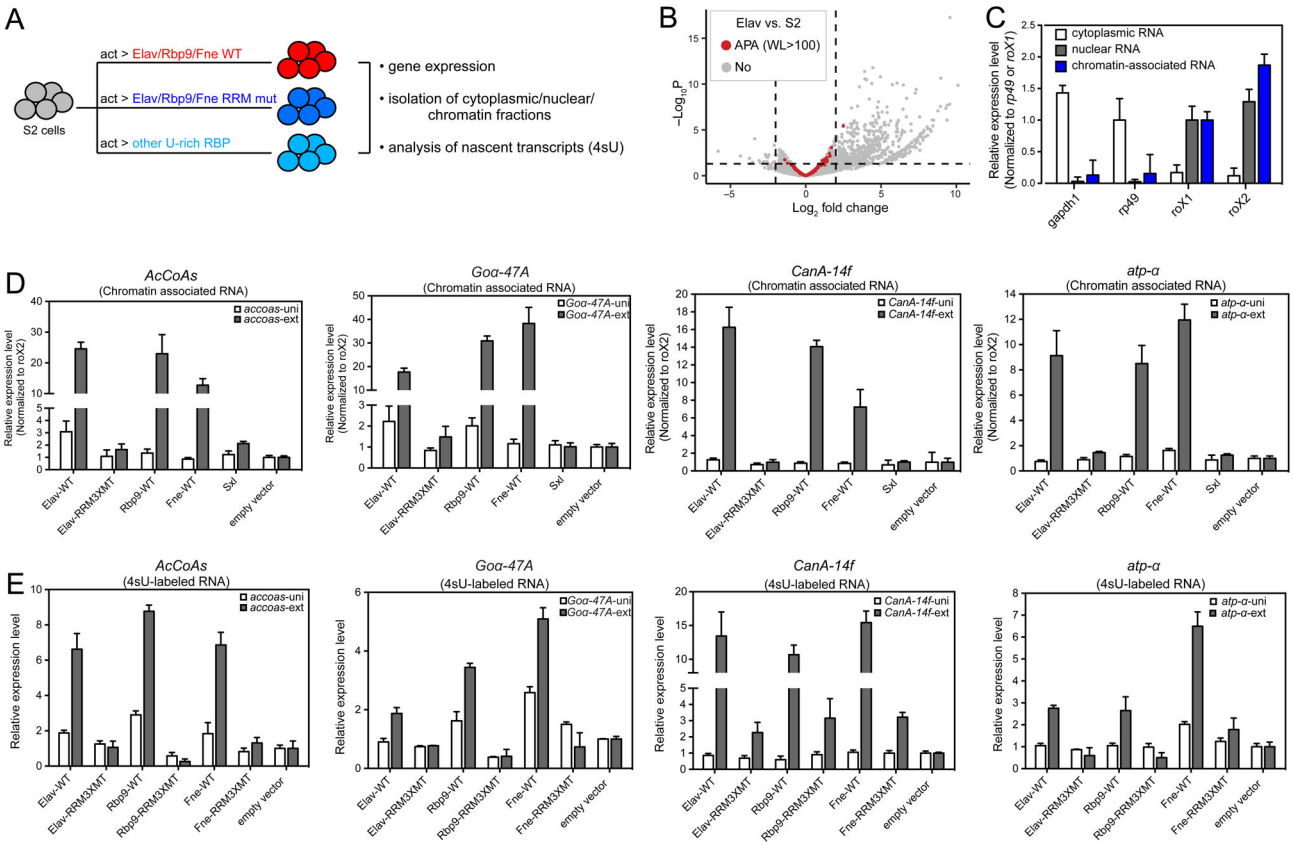

Figure 4. ELAV/Hu family RBPs induce distal 3’ UTR isoforms via nascent transcripts.

(A) Experimental scheme. S2R+ cells were transfected with wildtype or 3xRRM-mut versions of ELAV/Hu factors, or with control U-rich RBP, and processed for gene expression analysis from total RNA, cell fractionated RNAs, or from nascent transcribed RNAs. (B) Volcano plot showing $\log_2$FC (determined by aggregate 3’-seq data across isoforms) between control and Elav WT-expressing S2R+ cells; genes with change in 3’ UTR weighted length (ΔWL) ≥ 100nt are marked in red. Genes whose 3’ UTRs were extended by Elav did not show substantial or directional change in total levels. Similar findings were made for Rbp9 and Fne overexpression (Supplementary Figure 6). The regions are divided by a dashed bar indicates genes exhibiting >4-fold change at a p<0.05. (C) Validation of cell fractionation experiments. qRT-PCR analysis shows enrichment of mRNA transcripts in cytoplasm and roX transcripts in nucleus (mean ± SD, n = 3). (D) Wildtype Elav/Rbp9/Fne induce the accumulation of neural-like 3’ UTR extensions in chromatin-associated RNAs, while mutant Elav or wildtype Sxl do not. Relative expression level of universal (uni) and extension (ext) isoforms were calculated by normalizing raw Ct values to *roX2* (mean ± SD, n = 3). (E) Analysis of nascent 4sU-labeled transcripts. Wildtype Elav/Rbp9/Fne specifically induce the accumulation of 3’ UTR extensions in newly-synthesized RNAs. Relative expression level was calculated by normalizing raw Ct values to *roX2* (mean ± SD, n = 3). See also Figures S4–5.

Author Manuscript Author Manuscript Author Manuscript Author Manuscript

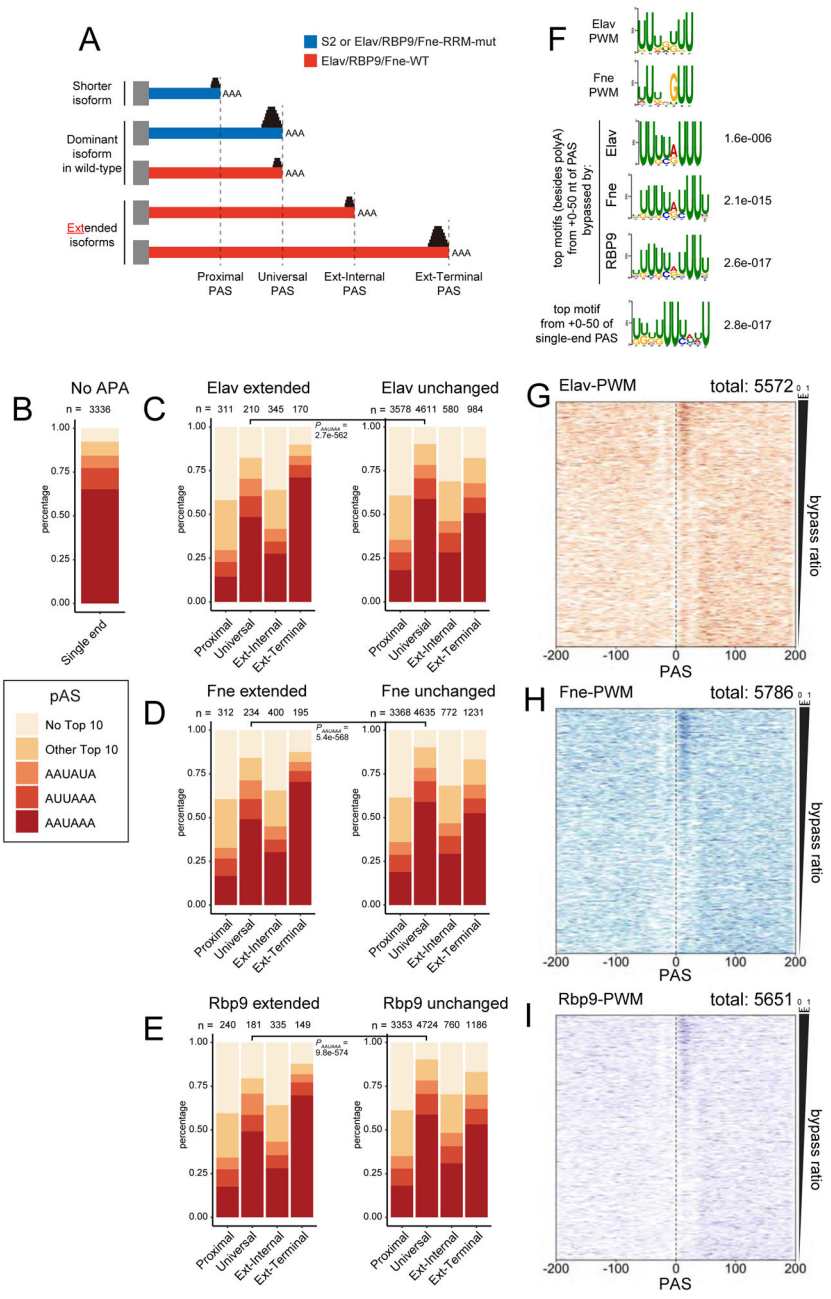

Figure 5. ELAV/Hu RBPs mediate bypass of weak proximal polyA sites bearing ELAV motifs

(A) Analysis scheme of alternative polyA sites. We divided polyA sites (CPM>5) in S2R+ cells into the designated categories, in order to derive their distinct properties in genes that were or were not responsive to ectopic ELAV/Hu RBPs. (B-E) Calculation of polyA signal (PAS) type. The darker colors from bottom of each stacked plot represent the two optimal PAS in *Drosophila*, AAUAAA and AUUAAA, with less frequent PAS types noted. (B) Genes with single ends (non-APA loci), even in the presence of ectopic Elav/Fne/Rbp9, exhibit high frequency of canonical PAS. (C-E) PAS analysis of multi-end genes, segregated according to responsiveness to Elav (C), Fne (D) or Rbp9 (E). APA genes that are not responsive to ectopic ELAV/Hu factors exhibit higher frequencies of optimal PAS in their

Author Manuscript Author Manuscript Author Manuscript Author Manuscript

dominant universal PAS, compared to APA genes that are lengthened by Elav/Fne/Rbp9 (note blue brackets for comparison). (F) De novo motif analysis of +0–50 nt of PAS sites that are bypassed by ectopic Elav/Fne/Rbp9 shows strong enrichment for a U-rich motif that closely resembles the *in vitro* selected sequences for Elav and Fne. Note that a distinct downstream U/GU-rich motif is enriched downstream of PAS of single-end genes, which more closely resembles the CstF64 site. (G-I) Positional enrichment of ELAV/Hu binding sites. Shown are locations of 80% matches to Elav (G), Fne (H) or Rbp9 (I) *in vitro* selected position weight matrices (PWMs), sorted by the relative amount of PAS bypass induced by ectopic ELAV/Hu factors. ELAV/Hu binding sites are preferentially enriched downstream of PAS that are bypassed by these RBPs.

Author Manuscript Author Manuscript Author Manuscript Author Manuscript

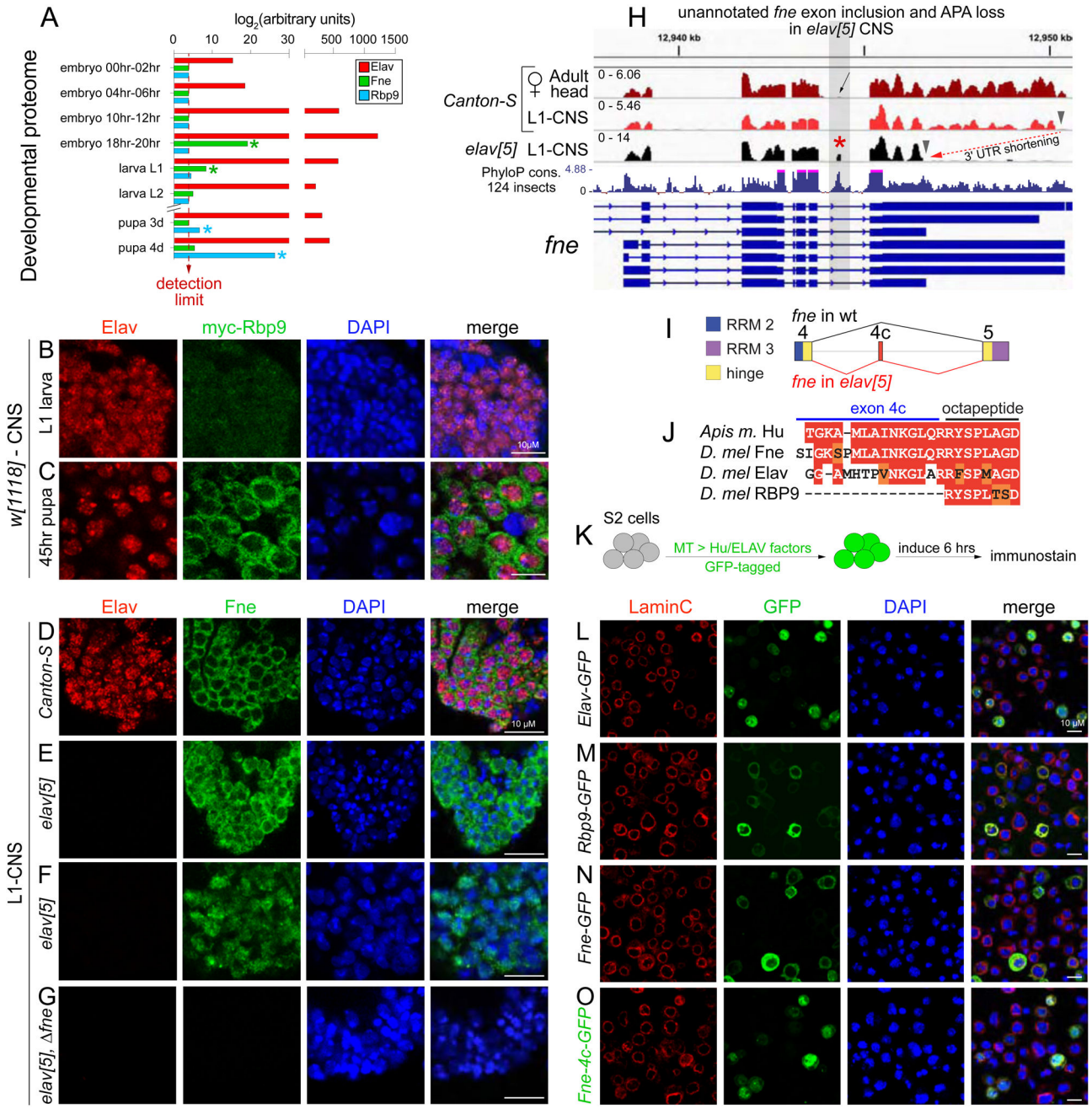

Figure 6. Relocalization of Fne from cytoplasm into the nucleus of *elav* mutant neurons.

(A) Developmental proteome data from selected embryo and larval stages shows that Elav is by far the dominant ELAV/Hu protein detected in embryos, but Fne accumulates by the end of embryogenesis. Rbp9 peptides were barely scored above the detection limit across this timecourse. (B-C) A BAC genomic transgene bearing 3xmyc-tags into *rbp9* shows almost no expression in L1-CNS (B), but abundant cytoplasmic expression in 45 hour pupal CNS (C). (D-G) Immunostainings of Elav (red) and Fne (green) in *Canton-S* control (D), *elav* mutant (E-F), and *elav, fne* double mutant (G) L1 CNS. In wildtype (D), Elav is predominantly nuclear while Fne is mostly in the cytoplasm. We can judge the specificity of these antibody

Author Manuscript Author Manuscript Author Manuscript Author Manuscript

signals by parallel CNS staining of the respective deletion alleles (E-G). Note that in *elav* mutant CNS, Fne is now substantially detected in nucleus (E), with certain neurons showing strongly nuclear Fne (F). (H) RNA-seq data showing the appearance of an unannotated *fne* exon in *elav* mutant CNS (asterisk); this exon is nominally detected in adult head (arrow) but is highly conserved (PhyloP track). *fne* also undergoes APA shortening in *elav* mutants. (I) Schematic of the *fne* microexon, termed 4c. (J) Fne exon 4c inserts sequence adjacent to the octapeptide within the hinge region; this unannotated isoform is identical to a sequence encoded by the sole ELAV/Hu locus in *Apis mellifera* (honeybee). (K) Strategy to test subcellular localization of *Drosophila* ELAV/Hu factors and isoforms. (L-O) Representative fields of transfected S2R+ cells stained for nuclear membrane marker LaminC (red), endogenous GFP for ELAV/Hu fusion proteins (green) and DAPI (blue). (L) Elav is predominantly nuclear, while Rbp9 (M) and Fne (N) are predominantly cytoplasmic. (O) Fne-4C bearing the microexon is predominantly nuclear. See also Figure S6.

Author Manuscript Author Manuscript Author Manuscript Author Manuscript

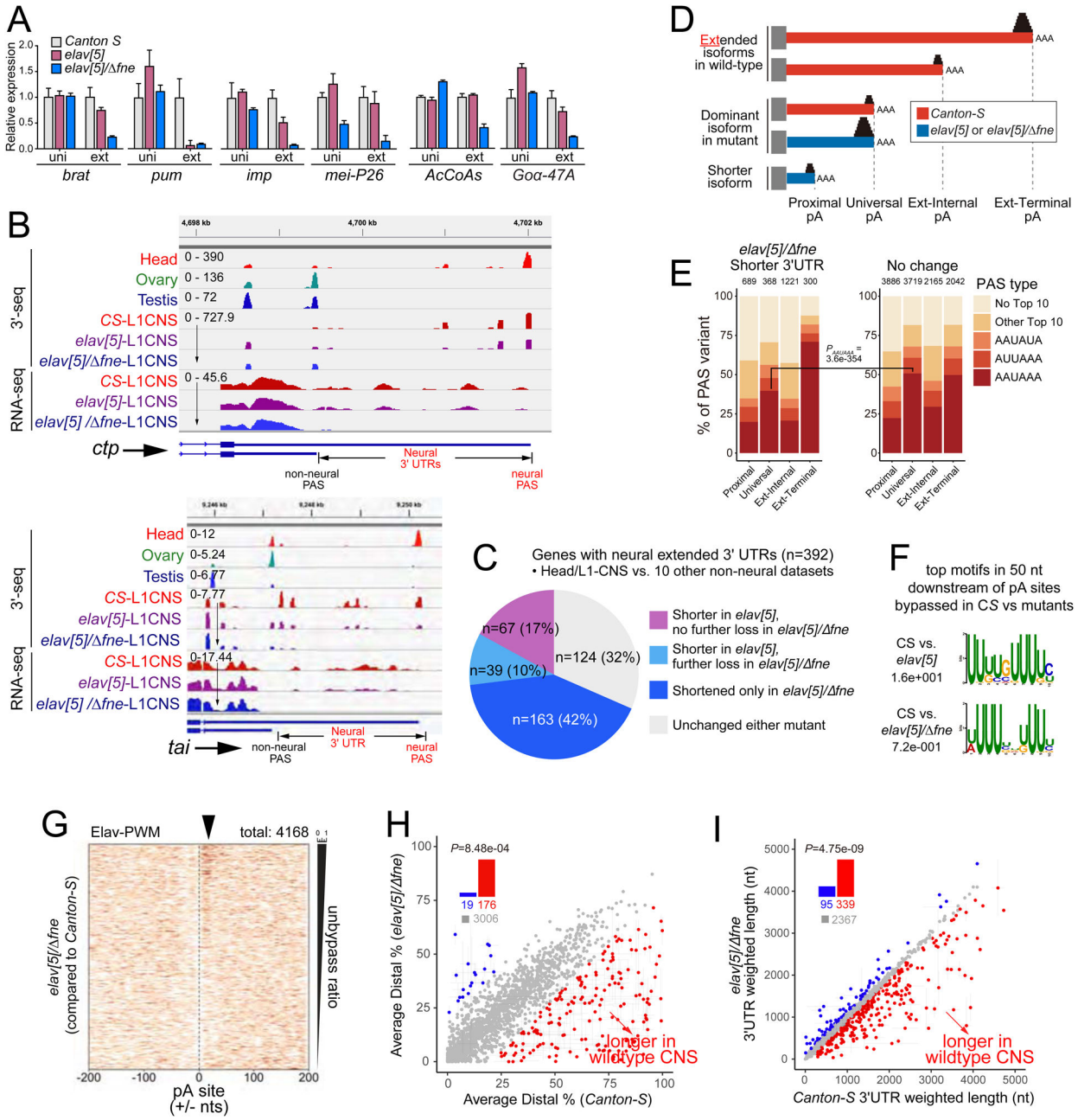

Figure 7. Overlapping activities of Elav and Fne specify the neural 3' UTR extension landscape.

(A-B) qRT-PCR analysis of universal (uni) and extended (ext) 3' UTR amplicons of neural APA loci in 1st instar larvae. Relative expression level was calculated by normalizing raw Ct values from control *Canton-S* and mutants (*Δfne*, *elav[5]*, or *elav[5]/Δfne* double) to *rpl14* (mean ± SD, n = 3). (A) Neural 3' UTR extensions are maintained in *fne* mutants. (B) The *pum* 3' UTR extension is dependent on Elav alone, and is not further decreased in double mutants. By contrast, the other tested loci require joint activity of Elav/Fne to accumulate neural 3' UTR isoforms. (C) IGV screenshots of RNA-seq and 3'-seq data from wildtype and mutant dissected L1 CNS. These genes illustrate that neural-specific 3' UTRs in L1-CNS (judged by comparison with other 3'-seq data from tissues such as head, ovary and

Author Manuscript Author Manuscript Author Manuscript Author Manuscript

testis) are generally only fully lost in *elav[5]/Δfne* double mutants. (D) Genetic dependency of neural 3' UTR extensions on Hu factors. Two-thirds of the neural extension landscape is lost in single and/or double mutants, with the strong majority of these dependent on both Elav/Fne. (E) Scheme to categorize PAS between wildtype and mutant L1 CNS. (F) Genes that show loss of 3' UTR extensions in *elav[5]/Δfne* mutants exhibit moderately weaker core PAS at their universal termini. (G) De novo motif analysis of universal PAS at genes that lose neural 3' UTR extension isoforms in *elav[5]* or *elav[5]/Δfne* mutants shows enrichment of downstream ELAV/Hu-binding site motifs. (H) Positional enrichment of ELAV/Hu-motifs downstream of proximal/universal PAS is found preferentially in genes that lose neural 3' UTR extension isoforms in *elav[5]/Δfne* mutants. (I) Global loss of neural 3' UTR extension isoforms in *elav[5]/Δfne* mutants. This plot shows the average expression of distal isoforms across replicates; the range is shown for genes with >20% differential usage in distal 3' UTRs (blue=shorter in wildtype, red=longer wildtype). The trend for directional 3' UTR shortening in *elav[5]/Δfne* mutants is significant ($p = 6.26\ e^{-03}$; Student's *t*-test). (J) Double deletion of *elav/fne* results in a major shift in 3' UTR sizes. Shown are the weighted 3' UTR lengths across isoforms for each gene (the plot has been truncated at 5kb, note that some 3' UTRs are longer than this). Many genes have lost >1 kb of 3' UTR in the CNS of *elav[5]/Δfne* mutants and some have lost multi-kb 3' UTRs. See also Figures S7–8.

Author Manuscript Author Manuscript Author Manuscript Author Manuscript

KEY RESOURCES TABLE

REAGENT or RESOURCE	SOURCE	IDENTIFIER
Antibodies		
Mouse monoclonal to Flag	Sigma-Aldrich	Cat# F3165, RRID: AB_259529
Mouse monoclonal to HA, HRP conjugated	Sigma-Aldrich	Cat# H6533, RRID: AB_439705
Mouse monoclonal to beta-tubulin	Developmental Studies Hybridoma Bank	Cat# E7, RRID: AB_2315513
Mouse monoclonal to HP1	Developmental Studies Hybridoma Bank	Cat# C1A9, RRID: AB_528276
Mouse monoclonal to Lamin C	Developmental Studies Hybridoma Bank	Cat# LC28.26, RRID: AB_528339
Mouse monoclonal to c-Myc	Sigma-Aldrich	Cat# M4439, RRID: AB_439694
Rat monoclonal to Elav	Developmental Studies Hybridoma Bank	Cat# Elav-7E8A10, RRID: AB_528218
Mouse monoclonal to Elav	Developmental Studies Hybridoma Bank	Cat# Elav-9F8A9, RRID: AB_528217
Rat monoclonal to Fne	Gift from Marie Laure Samson lab	N/A
Rabbit polyclonal to GFP	Molecular Probes	Cat# A-11122, RRID: AB_221569
Polyclonal Goat Anti-mouse Immunoglobulins with HRP	Jackson ImmunoResearch Labs	Cat# 115–036-062, RRID: AB_2307346
Polyclonal Goat Anti-rat Immunoglobulins with HRP	Jackson ImmunoResearch Labs	Cat# 112–005-020, RRID: AB_2338093
Polyclonal Goat Anti-rabbit Immunoglobulins with HRP	Thermo Fisher Scientific	Cat# PA1–29391, RRID: AB_10978297
Goat anti-Mouse IgG (H+L) Alexa Fluor 546	Thermo Fisher Scientific	Cat# A-11018, RRID: AB_2534085
Goat anti-Rat IgG (H+L) Alexa Fluor 633	Thermo Fisher Scientific	Cat# A-21247, RRID: AB_141778
Bacterial and Virus Strains		
TOP10 Competent *E. coli*	Lab stock	
NEB® 5-alpha Competent *E. coli* (High Efficiency)	NEB	Cat# C2987
One Shot™ ccdB Survival™ 2 T1R Competent Cells	Invitrogen	Cat# A10460
Chemicals, Peptides, and Recombinant Proteins		
TRIzol Reagent	Invitrogen	Cat# 15596018
TRIzol-LS reagent	Invitrogen	Cat# 10296028
4-Thiouridine (4sU)	Sigma-Aldrich	Cat# T4509
EZ-Link™ HPDP-Biotin	Thermo Fisher Scientific	Cat# 21341
Dynabeads™ MyOne™ Streptavidin C1	Invitrogen	Cat# 65001
Oligo d(T)25 Magnetic Beads	NEB	Cat# S1419S
Glyoxal solution	Sigma-Aldrich	Cat# 128465
Poly-L-lysine solution	Sigma-Aldrich	Cat# P8920–100ML
Formaldehyde solution ACS reagent, 37 wt. % in H2O	Sigma-Aldrich	Cat# 252549–100ML
DAPI solution	Thermo Fisher Scientific	Cat# 62248
Normal goat serum	Sigma-Aldrich	Cat# G9023–10ML
VECTASHIELD® Vibrance Antifade Mounting Medium without DAPI	Vector Laboratories	Cat# H-1700–2
VECTASHIELD® Antifade Mounting Medium with DAPI	Vector Laboratories	Cat# H-1500–10

Author Manuscript Author Manuscript Author Manuscript Author Manuscript

REAGENT or RESOURCE	SOURCE	IDENTIFIER
SuperScript II reverse transcriptase	Invitrogen	Cat# 18064022
SuperScript III reverse transcriptase	Invitrogen	Cat# 18080093
PowerUp™ SYBR™ Green Master Mix	Applied Biosystems	Cat# A25742
Easy-tide ^{32}P-dCTP	PerkinElmer	Cat# NEG513H250UC
Critical Commercial Assays		
NEBuilder HIFI DNA assembly kit	NEB	Cat# E5520S
Q5 site-directed mutagenesis kit	NEB	Cat# E0554S
pENTR™/D-TOPO™ Cloning Kit	Invitrogen	Cat# K240020
Gateway™ LR Clonase™ II Enzyme mix	Invitrogen	Cat# 11791100
Amersham ECL Western Blotting Detection Kit	GE healthcare Life Sciences	Cat# RPN2108
TurboBlotter Kit and refills	GE healthcare Life Sciences	Cat# 10416316
Amersham Megaprime DNA Labeling System (for use with labeled dCTP)	GE healthcare Life Sciences	Cat# RPN1606
QuantSeq 3’ mRNA-Seq Library Prep Kit REV for Illumina	Lexogen	Cat# 016.24
QuantSeq PCR add-on kit	Lexogen	Cat# 020.96
TruSeq Stranded Total RNA with Ribo-Zero Human/ Mouse/Rat	Illumina	Cat# RS-122–2202
Experimental Models: Cell Lines and Flies		
Drosophila S2R+ cells	Drosophila Genomics Resource Center	N/A
D. melanogaster Canton-S	Drosophila Genomics Resource Center	N/A
D. melanogaster w sn ela v[5]/FM 7-DfdGFP	This study	N/A
D. melanogaster w fneΔ (mw+) elav[5]/FM7-DfdGFP	This study	N/A
D. melanogaster transgenic for 3xmyc-Rbp9 in Pacman CH322–140N12	Zaharieva, MCB 2015	
Deposited Data		
3’-end sequencing, RNA-seq and CLIP-seq datasets	All datasets generated in this study were deposited in NCBI-GEO GSE155534. Additional information can be found in Table S1.	
Raw files of immunoblots and northern blots	This study.	
Raw files of immunostaining	This study.	
Oligonucleotides and primers		
Oligodeoxyribonucleotides/pri mers are listed in Table S7	Eton Bioscience / IDT	N/A
Recombinant DNA		
pAc5.1 /V5-His C vector	Invitrogen	Cat# V411020
pGEM-T	Promega	Cat# A3600
pAc5.1C-GFP	Lab stock	N/A
pENTR™/D-TOPO™	Invitrogen	Cat# K240020
MT-GAx-CoPuro	Gift from Norbert Perrimon lab	N/A
Software and Algorithms		

Author Manuscript

Author Manuscript

Author Manuscript

Author Manuscript

REAGENT or RESOURCE	SOURCE	IDENTIFIER
Prism 7 for Mac OS X	GraphPad	https://www.graphpad.com
Fiji ImageJ 2.0.0-rc-68/1.52e	N/A	https://imagej.nih.gov/ij
RStudio Version 1.2.1335	Rstudio	https://rstudio.com/
IGV_2.6.3	Broad Institute	http://software.broadinstitute.org/software/igv/
HISAT2		doi: 10.1038/nmeth.3317